Theory of two magnon scattering microwave relaxation and ferromagnetic resonance linewidth in magnetic thin films

M. J. Hurben and C. E. Patton[a)]
Department of Physics, Colorado State University, Fort Collins, Colorado 80523

(Received 22 July 1997; accepted for publication 5 January 1998)

A detailed analysis of the two magnon scattering contribution to the microwave relaxation and ferromagnetic resonance linewidth in isotropic and anisotropic films and disks has been made. The analysis is based on the Sparks, Loudon, and Kittel (SLK) theory for the scattering of uniform mode magnons into degenerate spin wave states for isotropic spherical samples in the presence of magnetic inhomogeneities in the form of spherical voids or pores. The SLK theory has been extended to include: (i) thin film and thick film samples magnetized in an oblique out-of-plane direction; (ii) uniaxially anisotropic materials with either easy-axis or easy-plane anisotropy and an anisotropy axis perpendicular to the disk plane; (iii) a modified density of degenerate states to account for the nonzero relaxation rate of the scattered spin waves; and (iv) two limiting cases of the scattering interaction: (a) the original SLK case where the inhomogeneities are modeled as spherical voids and the coupling to the degenerate spin waves varies with the spin wave propagation direction and (b) an isotropic scattering model where the coupling is independent of the propagation direction. The formulation is valid for thick films for which the discrete nature of the spin wave modes may be neglected. The two magnon linewidth as a function of field orientation is calculated for three classes of material parameters corresponding to yttrium iron garnet and barium M-type and zinc Y-type hexagonal ferrites. The linewidth versus static field angle profiles show characteristic profiles which depend on the crystalline anisotropy, the sample dimensions, the nature of the scattering interaction, the inhomogeneity size, and the inhomogeneity volume fraction. These parameters, as well as the shape and evolution of the spin wave band as a function of the field angle under ferromagnetic resonance conditions, play critical roles in determining the linewidth versus angle profiles. © *1998 American Institute of Physics.* [S0021-8979(98)01208-0]

I. INTRODUCTION

The discovery of yttrium iron garnet (YIG)[1] has led to many advances in the fundamental understanding of magnetic materials. From a technological point of view, the most important of these properties concerns the losses which limit the high speed switching of the magnetization for memory elements and control the insertion loss for microwave devices. The basic loss mechanisms for such high frequency processes in YIG and related ferrite materials are best examined by microwave techniques at ferromagnetic resonance (FMR) as well as off resonance.[2] The main microwave loss mechanisms which are usually operative in ferrite materials have been reviewed in detail by Sparks.[3]

In addition to so-called ''intrinsic'' mechanisms in very pure, high quality single crystals of YIG materials, which yield FMR half power field swept linewidths in the 0.05 Oe/GHz range at room temperature and in the mOe range at low temperature, there are two other generic processes which tend to increase the microwave losses above these ''intrinsic'' levels. The first such ''nonintrinsic'' process is often termed ''two magnon scattering.'' The second nonintrinsic process is related to impurities. The present article is concerned with two magnon scattering.

A. Two magnon scattering losses and inhomogeneities

In ferromagnetic resonance, the two magnon scattering process involves coupling between the uniform mode and spin waves over a range of wave vectors which are degenerate with the microwave pump and the FMR response. The coupling is typically strongest for spin wave wavelengths which are on the order of whatever inhomogeneities may be present in the material. This process is termed ''two magnon scattering'' because the mechanism can be expressed theoretically by a second quantization formalism in which a uniform precession or FMR magnon is destroyed and a spin wave magnon at the same frequency is created. In the early theories,[4–7] the uniform mode source magnons and the spin waves were taken to be degenerate. Since the participating magnons (i) are degenerate and (ii) have different wave vectors, momentum is not conserved for the two magnon scattering process. From a formal point-of-view, the pseudomomentum from the spatial variation in the internal fields of one sort or another which derives from the inhomogeneities serves to conserve the momentum in the scattering calculation. Two magnon scattering requires, therefore, the presence of inhomogeneities. Later theories included the possible effects of secondary scattering.[8,9]

The two magnon scattering contribution to the FMR linewidth has been investigated theoretically and experimen-

a)Electronic mail: patton@lamar.colostate.edu

 © 1998 American Institute of Physics

tally for three types of inhomogeneities in bulk YIG, namely, surface pits, volume pores or voids, and randomly distributed single crystal grains in a polycrystal.[4,7] The most detailed published theory is for scattering due to an isolated spherical pore imbedded in a large sample.[3,4] Theoretical and experimental results have been reviewed in Ref. 2.

Critical evidence for the importance of two magnon scattering is contained in the data of Buffler[10] on linewidth versus frequency for YIG spheres which were polished to produce pits of different sizes. Various studies of FMR linewidths in ferrite materials have also demonstrated that detailed information on the two magnon scattering contribution to the loss may be obtained if the number of spin waves which are degenerate with the FMR frequency can be adjusted experimentally through the use of different sample shapes, different field orientations, etc.[11–14]

B. Thin films and degenerate spin waves

A considerable amount of related work has been done on thin films. Ferromagnetic resonance measurements in thin permalloy films,[15,16] for example, demonstrated the potential importance of two magnon scattering processes through the use of the thin film geometry and field orientation to change the degeneracy condition. For FMR with an in-plane static magnetic field and an in-plane magnetized thin film, there are a large number of spin wave states which are degenerate with the uniform mode and a significant contribution to the two magnon scattering linewidth is possible. If the static magnetic field is perpendicular to the film and sufficient to saturate the magnetization perpendicular to the film, there are essentially no spin wave states degenerate with the FMR frequency and there should be almost no two magnon scattering contribution to the linewidth. For an obliquely magnetized film, the FMR frequency lies between these two limits. The number of degenerate spin waves to which the uniform mode can couple via the two magnon process, and hence the relaxation rate and the linewidth, are strongly dependent on the external field orientation.

The angle dependence of the two magnon scattering contribution to the linewidth for films has been treated previously by Sparks.[17] This treatment was done for two limited cases, and only for isotropic materials. The first part of Sparks' treatment developed an approximate expression for the linewidth due to scattering from such spherical voids within the film, but did not explicitly consider the role of the void size. The second part considered scattering from large etch pits which extended through the film thickness. This work shows the wealth of two magnon effects which are important for thin films.

C. Objective of this work

The objective of this work is to provide a specific, analytical, and operational theoretical formalism for two magnon scattering relaxation and the FMR linewidth in thin films. A summary of the theory is given in Ref. 18.

The analysis is based on the transition probability calculation of Sparks, Loudon, and Kittel[4] (SLK) for isotropic spherical samples. In this approach, the microstructure is modeled in terms of spherical voids or pores. The calculation results in a relaxation rate expression which reflects the assumption of spherically symmetric inhomogeneities. While it is possible to extend the analysis to include nonspherical inhomogeneities,[17,19,20] no attempt has been made to include such effects here. For a wide distribution of pore or void shapes, it is reasonable to adopt an ''isotropic scattering'' limit in which the angular coupling term which derives from the dipole field distribution around a spherical void is replaced by some average value. The ''spherical void scattering'' and ''isotropic scattering'' limits give very different two magnon linewidth versus field angle profiles. These differences will provide a way to separate very different kinds of scattering processes.

Previously two magnon analyses have been limited to materials which were either isotropic or with relatively small levels of magnetocrystalline anisotropy such that the behavior of the spin wave band was essentially the same as for isotropic materials. Schlömann *et al.*,[21] among others, has shown that anisotropy can have a significant effect on the spin wave dispersion and the corresponding spin wave band. Explicit examples of such effects and further references may be found in Refs. 21–24.

The modifications in the spin wave band due to anisotropy have a large effect on the two magnon linewidth versus angle profiles. From a technological point of view, these effects are extremely important. This is due, in part, to the continuing interest in hexagonal ferrite materials for millimeter-wave device applications,[25] and the recent development of pulse laser deposited (PLD) single crystal barium ferrite (Ba–M) films.[26] These new Ba–M PLD films, as well as other PLD ferrite films,[27,28] have rather large FMR linewidths. As these materials are developed and refined for millimeter-wave device applications, it will be important to consider the possibility of a two magnon scattering contribution to the high frequency losses, the types of microstructure responsible for these losses, and ways to modify the film morphology to eliminate these effects and reduce the losses.

The objective of this work, then, has been: (i) to develop a clear, practical, and operational formalism for the two magnon scattering relaxation rate in anisotropic ferrite films; (ii) to make explicit the role of different types and sizes of inhomogeneities on the two magnon losses; (iii) to make explicit the role of anisotropy modifications to the spin wave band on these processes; and (iv) to provide example calculations of profiles of linewidth versus external field angle which demonstrate these effects.

Section II defines basic parameters and establishes operating equations for static equilibrium and the uniform mode FMR response when the static magnetic field is applied at some angle θ relative to the film normal. Section II also establishes operational equations for the FMR frequency, various effective field parameters, and a phenomenological relaxation rate which will be used to characterize intrinsic losses. Section III provides a brief review of spin wave properties for isotropic and uniaxially anisotropic materials. In Sec. IV, the relaxation rate or inverse relaxation time for scattering between the uniform mode and the degenerate spin waves is developed along the same lines as used in the origi-

nal SLK theory. Here, however, specific working equations are obtained for scattering into a band of spin waves of nonzero width. In Sec. V, these working equations are used to calculate the two magnon linewidth as a function of the external field orientation for representative cases of isotropic, easy-axis, and easy-plane ferrite films and disks, and a variety of microstructure options which correspond more-or-less to those expected in real materials.

II. UNIFORM MODE ANALYSIS

This section considers various aspects of the uniform mode response in thin film ferromagnetic resonance. The key topics are (i) static equilibrium, (ii) dynamic response and effective fields, (iii) FMR field as a function of static field angle relative to the film normal at fixed frequency, and (iv) FMR linewidth versus angle for fixed frequency and fixed relaxation rate. The dynamic response analysis is based on the Kittel[29] formulation of ferromagnetic resonance and relaxation according to the Bloch–Bloembergen formulation.[30] The effect of anisotropy is included through a free energy approach.

Example results are given for YIG, Ba–M, and Zn–Y materials. Because it has a relatively small cubic anisotropy, YIG is treated as an isotropic material. The hexagonal ferrites, on the other hand, exhibit large uniaxial anisotropies, with the easy direction along the c axis for Ba–M and in the c plane for Zn–Y. For these materials, the c axis is taken to be oriented normal to the disk. This uniaxial anisotropy may be characterized in terms of a anisotropy energy density of the form $E_K=-K_U\cos^2\phi$, where K_U is the uniaxial anisotropy energy density in erg/cm^3 and ϕ is the angle between the magnetization vector $\mathbf{M}$ and the c axis. Positive K_U corresponds to an easy axis material with the easy $\mathbf{M}$ direction along the disk normal. Negative K_U corresponds to an easy plane material with the easy $\mathbf{M}$ direction in the disk plane. It will prove convenient to define an effective anisotropy field $H_A=2K_U/M_s$, where M_s is the saturation magnetization of the material in emu/cm^3. Positive values of the anisotropy field H_A correspond to easy-axis anisotropy and negative values to easy-plane anisotropy. An H_A value of zero corresponds to an isotropic material. Typical room temperature values of H_A for hexagonal ferrite materials are 16.3 kOe for Ba–M and -9.0 kOe for Zn–Y.[31] Typical values of the room temperature saturation induction $4\pi M_s$ are 1.75 kG for YIG, 4.7 kG for Ba–M, and 2.1 kG for Zn–Y.[31] Gaussian units will be used throughout this work.

A. Sample geometry and static equilibrium

Consider a thin, uniaxially anisotropic disk or film magnetized by the application of an external static magnetic field. Figure 1 shows the sample oriented relative to some right-handed X-Y-Z frame such that the sample normal is parallel to the Z axis. This direction also corresponds to the uniaxial crystalline c axis. The disk is assumed to have symmetry about the c axis and to be characterized by the in-plane and out-of-plane demagnetization factors N_{XY} and N_Z which satisfy the condition $N_Z+2N_{XY}=1$. A static external magnetic field $\mathbf{H}_{\text{ext}}$ is applied at an angle θ relative to the sample normal and is taken to lie in the Y-Z plane. At static equilibrium, the static magnetization vector $\mathbf{M}_s$ also lies in the Y-Z plane and is directed at an angle ϕ relative to the sample normal. The specific situation in Fig. 1 would apply to an isotropic material, an easy-plane material with $H_A<0$, or an easy-axis material with $H_A<4\pi M_s$. For a Ba–M disk with easy-axis anisotropy and $H_A>4\pi M_s$, the magnetization angle ϕ would be less than the field angle θ.

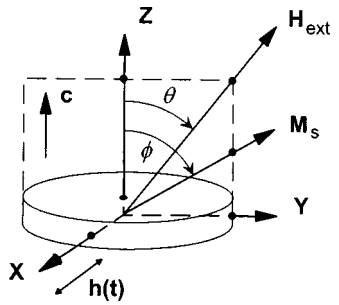

FIG. 1. Disk, field, and static magnetization geometry for the static equilibrium and FMR analysis. The external field $\mathbf{H}_{\text{ext}}$ is applied at an angle θ relative to the sample normal and crystalline c axis and lies in the Y-Z plane. The static magnetization $\mathbf{M}_s$ lies in the Y-Z plane at an angle ϕ relative to the Z axis.

The condition for static equilibrium is found if the net torque on $\mathbf{M}_s$ is set equal to zero. The net torque is a result of the external field, the demagnetization field, and the anisotropy which acts to pull the magnetization into an easy direction. This condition yields an expression which relates the field and magnetization angles θ and ϕ

$$4H_{\text{ext}}\sin(\theta-\phi)=[4\pi M_s(1-3N_Z)+2H_A]\sin(2\phi). \tag{1}$$

Note that for $H_{\text{ext}}>|H_A|$, the internal field and magnetization vectors will be parallel with $\mathbf{H}_{\text{ext}}$ applied either perpendicular to the disk, with $\phi=\theta=0°$, or in-plane, with $\phi=\theta=90°$.

B. Dynamic response, relaxation, and effective fields

In the small signal limit, the condition $|\mathbf{m}(t)|\ll M_s$ is satisfied and the total time dependent magnetization vector $\mathbf{M}(t)$ may be resolved into a static component oriented parallel to the saturation magnetization vector $\mathbf{M}_s$ and a small dynamic component $\mathbf{m}(t)$ perpendicular to $\mathbf{M}_s$

$$\mathbf{M}(t)\approx\mathbf{M}_s+\mathbf{m}(t). \tag{2}$$

In the uniform mode analysis, $\mathbf{m}(t)$ is assumed to be independent of position throughout the sample.

The precessional motion of the total magnetization vector about the equilibrium direction can be driven by the application of a microwave field $\mathbf{h}(t)$ perpendicular to the static magnetization direction. The microwave field is taken to be uniform throughout the sample, to vary sinusoidally with a frequency ω, and to be directed along the X axis in Fig. 1. This insures that $\mathbf{h}(t)$ will be perpendicular to $\mathbf{M}_s$ regardless of the angles θ and ϕ. Ferromagnetic resonance results when the microwave frequency corresponds to the natural frequency of the precession.

There are two standard ways to perform the FMR experiment. In the first approach, the static field $\mathbf{H}_{\text{ext}}$ is applied at some angle θ and held at a fixed strength while the pump

frequency ω is varied. The response is then characterized by the FMR frequency ω_{FMR} at which the maximum power is absorbed and a corresponding frequency linewidth $\Delta\omega$. This linewidth is the interval, in frequency units, between the half-power points of the microwave absorption profile.

In the second approach, and the one which is favored experimentally, the microwave frequency is fixed at ω while the strength of the external field $\mathbf{H}_{\mathrm{ext}}$ is varied. The two basic parameters of interest are then the FMR field H_{FMR} and field linewidth ΔH. The field H_{FMR} is defined to be the value of H_{ext} at which the maximum microwave power is absorbed. The linewidth ΔH is the interval, in field units, between the half power points.

In order to determine the FMR parameters ω_{FMR}, H_{FMR}, $\Delta\omega$, and ΔH, a modified version of the torque equation is often used. The modification involves the addition of phenomenological damping terms which account for the relaxation of the magnetization. The analysis leads to relatively simple working equations for the FMR frequency ω_{FMR} and linewidth $\Delta\omega$. Expressions for the corresponding field parameters H_{FMR} and ΔH are much more involved. Determination of these parameters is discussed shortly.

The two most commonly used phenomenological modifications to the torque equation which account for loss are the Bloch–Bloembergen (BB)[30] and Landau–Lifshitz (LL)[32] approaches. In this work, the BB formalism will be used exclusively, because it is physically consistent with the two magnon process. A thorough discussion of the various relaxation mechanisms and the phenomenological damping formalisms is given by Sparks.[3] Various phenomenological damping approaches to ferromagnetic resonance are also discussed by Lax and Button[33] and Patton.[2]

The modified torque equation of motion for the transverse dynamic magnetization $\mathbf{m}(t)$ with BB loss included may be written as

$$\frac{d\mathbf{m}(t)}{dt} = -\gamma\mathbf{M}(t)\times\mathbf{H}(t) - \frac{\mathbf{m}(t)}{2T}. \tag{3}$$

Here $\mathbf{H}(t)$ represents the total effective magnetic field in the sample, γ is the absolute value of the electron gyromagnetic ratio, and $1/T$ is the transverse and longitudinal BB relaxation rates. A typical value for γ is 1.76×10^7 rad/s Oe or 2.8 GHz/kOe in practical units. For a thin disk or film magnetized out-of-plane, a $1/T$ value of 1.76×10^7 rad/s would correspond to a field swept linewidth of 1 Oe. Note that $1/T$ is in units of rad/s. The calculations presented below will yield expressions for $1/T$. When numerical results are presented, these will be given in terms of $1/\gamma T$, in Oe, corresponding to field linewidths. The BB formulation also includes a longitudinal relaxation term for the z component of the total dynamic magnetization. This term is not considered in a linear theory.

The net magnetic field $\mathbf{H}(t)$ consists of the applied fields $\mathbf{H}_{\mathrm{ext}}$ and $\mathbf{h}(t)$ along with the static and dynamic fields which result from sample demagnetization and non-Maxwellian effective fields related to magnetocrystalline anisotropy. The net effective field $\mathbf{H}(t)$ can be expressed in terms of a modified demagnetizing tensor $\mathbf{A}$ according to

$$\mathbf{H}(t) = \mathbf{H}_{\mathrm{ext}} + \mathbf{h}(t) + \mathbf{A}\cdot\mathbf{M}(t). \tag{4}$$

In the X-Y-Z frame, the tensor $\mathbf{A}$ is given by

$$\mathbf{A} = \begin{pmatrix} -4\pi N_{XY} & 0 & 0 \\ 0 & -4\pi N_{XY} & 0 \\ 0 & 0 & -4\pi N_Z + \dfrac{H_A}{M_s} \end{pmatrix}. \tag{5}$$

For purposes of the usual uniform mode analysis, the components of the dynamic magnetization are assumed to have an $e^{i\omega t}$ dependence. The analysis leads to an expression for the FMR frequency ω_{FMR} which is valid to first order in the loss term $1/T$

$$\omega_{\mathrm{FMR}} = \gamma(H_x H_y)^{1/2}, \tag{6}$$

$$H_x = H_{\mathrm{ext}}\cos(\theta-\phi) + \tfrac{1}{2}[2H_A - 4\pi M_s(3N_Z-1)] \times\cos^2\phi, \tag{7}$$

$$H_y = H_{\mathrm{ext}}\cos(\theta-\phi) + \tfrac{1}{2}[2H_A - 4\pi M_s(3N_Z-1)] \times\cos(2\phi). \tag{8}$$

The H_x and H_y parameters may be viewed as effective stiffness fields which characterize the instantaneous torque exerted on $\mathbf{M}(t)$ when it is tipped parallel toward the $\mathbf{h}(t)$ direction or perpendicular to the $\mathbf{h}(t)$ direction, respectively.

Although the above results give ω_{FMR} as a function of H_{ext}, the explicit dependence of the value of the external magnetic field, H_{FMR}, on the field angle θ for resonance at a given frequency ω, can also be determined. Once the sample parameters γ, $4\pi M_s$, H_A, and N_Z are specified, Eqs. (1), (6), (7), and (8), with H_{ext} and ω_{FMR} replaced by H_{FMR} and ω, respectively, can be solved for H_{FMR} as a function of θ.

C. FMR field versus angle at fixed frequency

Figure 2 shows the calculated FMR field H_{FMR} as a function of the external field angle θ for the three representative materials described above and in the infinite thin film limit where $N_Z=1$ is satisfied. Figure 2(a) is for YIG at $\omega/2\pi=10$ GHz, Figure 2(b) is for Ba–M at 50 GHz, and Figure 2(c) is for Zn–Y at 10 GHz. The frequencies were chosen to be representative of typical operating frequencies for these materials. These same material—frequency combinations will be used throughout this work for purposes of numerical evaluations.

Consider the YIG results in (a) first. For an external field applied perpendicular to the film plane at $\theta=\phi=0°$, the FMR field is a maximum, while the minimum occurs for the in-plane configuration at $\theta=\phi=90°$. The variation in H_{FMR} with the field angle is due to the change in the sample demagnetization and stiffness fields. For the Ba–M case in (b), the situation is reversed because of the very strong easy-axis anisotropy perpendicular to the film plane. Here, the FMR field is a minimum for $\theta=\phi=0°$, which corresponds to the easy direction, and a maximum when the field is in-plane, along a hard direction. For the Zn–Y result in (c), the anisotropy acts together with the demagnetization fields to pull the magnetization vector in-plane. For the out-of-plane orientation, the field required for ferromagnetic resonance is very

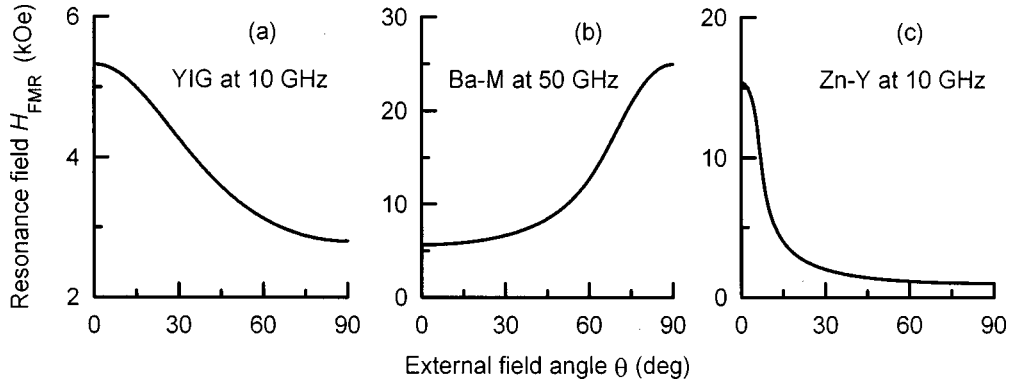

FIG. 2. Calculated static external field for ferromagnetic resonance, H_{FMR}, as a function of the external field angle θ for the three representative materials in the infinite thin film limit. (a) is for YIG at 10 GHz. (b) is for Ba–M at 50 GHz. (c) is for Zn-Y at 10 GHz.

large, but this field then rapidly decreases as the field is tipped away. The rapid change in H_{FMR} reflects the severe misalignment between the static field and magnetization vectors. For field angles above about 30° or so, the static magnetization is essentially in-plane.

The results in Fig. 2 demonstrate an important effect of the external field orientation on the FMR response for a constant microwave frequency, namely, that the strength of the applied static field and hence the net field within the material vary strongly with field angle. This effect will play a crucial role in the two magnon scattering and linewidth versus angle theory developed shortly.

D. Linewidth considerations and linewidth versus angle

The FMR analysis also yields an expression for the BB frequency swept linewidth $\Delta\omega$. This linewidth is conveniently expressed in magnetic field units as $\Delta(\omega/\gamma)$. The BB linewidth in field units is

$$\Delta(\omega/\gamma)=\frac{1}{\gamma T}. \tag{9}$$

In contrast with the FMR frequency result of Eq. (6), for which ω_{FMR} varied as the geometric mean of two stiffness fields, the BB linewidth $\Delta(\omega/\gamma)$ is constant and proportional to the transverse relaxation rate.

Unlike the simple $\Delta(\omega/\gamma)=1/\gamma T$ result of Eq. (9), a corresponding expression for the field swept linewidth ΔH in the field swept FMR experiment at constant frequency is much more complicated. This can be understood from an examination of the field and magnetization vectors during the course of an FMR experiment. For the frequency swept case, the orientation and strength of $\mathbf{H}_{\mathrm{ext}}$ are held fixed, so that the equilibrium direction of static magnetization $\mathbf{M}_s$ also remains constant. For the field swept case, the direction of $\mathbf{H}_{\mathrm{ext}}$ is fixed while its strength is varied. As can be seen from Eq. (1), the orientation angle ϕ for $\mathbf{M}_s$ will then vary as H_{ext} is swept, unless θ is either 0° or 90°. As a result, ΔH can be a complicated function of θ even for constant $1/T$. It will be seen from the two magnon scattering theory that the relaxation rate $1/T$ itself shows strong angle dependences as well. It is important from the outset, therefore, to separate and understand the geometric linewidth angle dependences which result in field swept experiments.

For a given $1/T$ value and a particular field angle θ, the field linewidth ΔH can be determined directly from the explicit microwave susceptibility expressions obtained from the uniform mode analysis. Although it is not possible to obtain simple closed form expressions for ΔH as a function of the field angle θ, it is possible to evaluate the susceptibility response numerically and determine ΔH as the separation in field values which correspond to the half-power points of the absorption. A simpler approach, and one which can be used to demonstrate the intuitive connections between ΔH and $\Delta(\omega/\gamma)$, is to invoke a simple connection between the two linewidths which is strictly valid only in the limit of small linewidths. This connection may be written as

$$\Delta H\approx\gamma\,\frac{\partial H_{\mathrm{FMR}}}{\partial\omega_{\mathrm{FMR}}}\,\Delta(\omega/\gamma). \tag{10}$$

The derivative can be determined from Eqs. (1), (6), (7), and (8). In the limit that $\Delta\omega\ll\omega_{\mathrm{FMR}}$ is satisfied, the linewidths predicted by the two approaches agree to within several Oe. As will be discussed below, the linewidth conversion factor $\gamma\partial H_{\mathrm{FMR}}/\partial\omega_{\mathrm{FMR}}$ is equal to one for $\theta=0°$, greater than one when magnetization rotation effects dominate the field swept line broadening at angles between $\theta=0°$ and $\theta=90°$, and is less than one for parallel resonance at $\theta=90°$.

The effect of the field orientation on the FMR linewidth for a constant relaxation rate is illustrated in Fig. 3. The figure follows the form of Fig. 2, with (a) for YIG, (b) for Ba–M, and (c) for Zn–Y. The calculations are based on the infinite thin film limit and the same material parameters and frequencies used in Fig. 2, along with $1/\gamma T$ values of 0.5, 20, and 15 Oe, for the YIG, Ba–M, and Zn–Y cases, respectively. These values correspond to reasonable out-of-plane resonance linewidths due to intrinsic losses in these materials at the chosen frequencies.

Consider the results for the YIG film in Fig. 3(a). Here, the field swept linewidth ΔH is equal to $1/\gamma T$ for the out-of-plane orientation and shows only a small increase at intermediate angles. There is a small but indiscernible drop in ΔH from $1/\gamma T$ at $\theta=90°$. In the case of YIG at 10 GHz, the

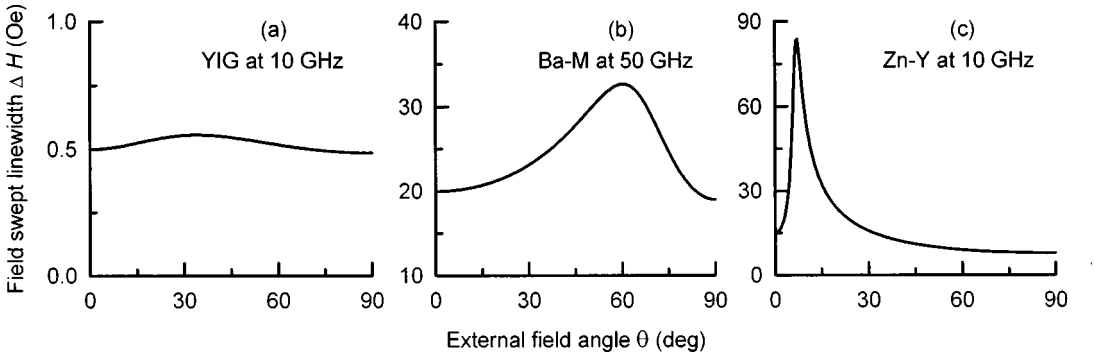

FIG. 3. Calculated ferromagnetic resonance field swept linewidth ΔH as a function of the external field angle θ for the three representative materials in the infinite thin film limit and for constant values of the BB relaxation rate $1/T$. (a) is for YIG at 10 GHz with $1/\gamma T = 0.5$ Oe. (b) is for Ba–M at 50 GHz with $1/\gamma T = 20$ Oe. (c) is for Zn–Y at 10 GHz with $1/\gamma T = 15$ Oe.

conversion factor between the field linewidth and the relaxation rate given by Eq. (10) is very close to one and essentially independent of angle. The small peak around $\theta = 35°$ is due to the small difference between the field angle θ and the magnetization angle ϕ as the field is rotated at intermediate angles. For in-plane ferromagnetic resonance at $\theta = \phi = 90°$, the YIG linewidth for BB damping is slightly smaller than the perpendicular linewidth at 0.47 Oe. This relative insensitivity of the YIG field swept linewidth to rotation is due to the near alignment of $\mathbf{M}_s$ with $\mathbf{H}_{\text{ext}}$ as the field is rotated and H_{ext} is maintained at the value needed for ferromagnetic resonance at 10 GHz.

The situation is quite different for the Ba–M linewidth results in (b) of Fig. 3. Here, the field swept linewidth shows a very significant variation with angle. Note that the large uniaxial anisotropy for the Ba–M film, with the easy axis perpendicular to the film, causes the FMR field to be small at $\theta = \phi = 0°$ and large at $\theta = \phi = 90°$. For intermediate θ values, the $\mathbf{M}_s$ vector tends to be somewhat closer to the film normal than does $\mathbf{H}_{\text{ext}}$ and the magnetization angle ϕ lags behind the field angle θ. For ferromagnetic resonance at 50 GHz and the combination of Ba–M parameters used here, the field swept linewidth for a constant $1/\gamma T$ values of 20 Oe increases to a maximum value of about 33 Oe near an external field angle of 60° and then drops to a value slightly below the perpendicular field linewidth at $\theta = \phi = 90°$.

As shown in (c), this effect is even more pronounced for Zn–Y film parameters and 10 GHz ferromagnetic resonance. In this case, the anisotropy is in-plane and serves to enhance the demagnetizing effects. Here, ΔH increases very rapidly as the external FMR field is rotated away from the perpendicular FMR orientation at $\theta = 0°$. The peak in ΔH occurs at $\theta \approx 8°$ and is more than a factor of 5 greater than the linewidth at $\theta = 0°$. It is important to keep in mind that the $1/\gamma T$ values in each of these calculations were taken to be constant, independent of θ.

It is instructive to compare the angle dependences of the linewidths in Fig. 3 with the angle dependences of the FMR fields shown in Fig. 2. It can be seen that the variation in the linewidth with the field angle roughly tracks the change in the slope of the H_{FMR} vs θ curve in each scenario.

III. SPIN WAVE DISPERSION AND DEGENERATE SPIN WAVES

This section presents a brief review of spin wave considerations which will be important for the two magnon process. Dispersion relations of spin wave frequency ω_k versus wave vector $\mathbf{k}$ are obtained. This section also provides an explicit examination of the change and frequency shift in the spin wave band for YIG, Ba–M, and Zn–Y films as one moves from the perpendicular FMR configuration with the field at $\theta = 0°$ to the parallel FMR case with the field at $\theta = 90°$. These considerations lead to an intuitive understanding of the change in the degenerate magnon situation and hence, the states available for two magnon scattering, as one moves from the perpendicular to the parallel FMR configurations. The presentation is limited to so-called bulk spin waves for which the wave number k is much greater than $2\pi/S$, where S is the film thickness. The magnetostatic mode limit in which k may be on the order of or smaller than $2\pi/S$, but still above the pure electromagnetic wave limit ω_k/c, where c is the speed of light, will not be considered here. Possible effects due to magnetostatic modes and film thickness effects other than demagnetizing factors will be briefly considered at the end of the article.

A. Classical bulk spin waves

For a bulk material, the sample boundaries can be taken to lie at infinity and do not influence the dispersive properties of the spin wave modes. For thin film materials, however, the boundary conditions of the magnetic field vectors can significantly modify these dispersion relations. Calculation of the so-called dipole-exchange modes, which are the normal modes for thin film materials, is in general extremely complicated and is beyond the scope of this work. References for dipole-exchange modes include Wolfram and De Wames,[34] De Wames and Wolfram,[35] and Kalinikos *et al.*[36]

In this work, the approach of Sparks[18] is followed. The bulk spin wave dispersion relations are used to approximate the normal modes of the film. This results in a considerable

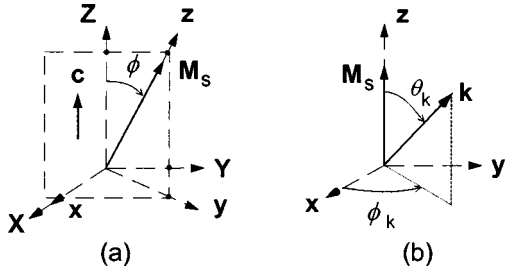

FIG. 4. (a) Relative orientations of the sample (X-Y-Z) and precessional (x-y-z) frames. The z axis is taken to be parallel to the static magnetization vector $\mathbf{M}_s$ and the x axis is taken to be parallel to the X axis. (b) Orientation of the propagation wave vector $\mathbf{k}$ relative to the x, y, and z axes in the precessional frame. The polar angle θ_k is measured relative to the z axis. The azimuthal angle ϕ_k is measured relative to the x axis.

simplification of the two magnon scattering analysis. As long as the microstructure responsible for the two magnon interaction is much smaller than the film thickness, the bulk spin wave dispersion relations provide a reasonable model for two magnon calculations.

In order to determine the bulk spin wave dispersion relations, Eq. (3) can be re-written in the lossless form, with the magnetization and field vectors taken to be functions of space as well as time

$$\frac{d\mathbf{m}(\mathbf{r},t)}{dt}=\gamma\mathbf{M}(\mathbf{r},t)\times\mathbf{H}(\mathbf{r},t). \tag{11}$$

Analogous to Eq. (2), the total magnetization is now of the form $\mathbf{M}(\mathbf{r},t)\approx\mathbf{M}_s+\mathbf{m}(\mathbf{r},t)$. The spatial dependences in the $\mathbf{H}(\mathbf{r},t)$ enter through the spatial dependence of $\mathbf{m}(\mathbf{r},t)$ and the associated dipole–dipole interactions, exchange interactions, and anisotropy considerations. These effects are considered shortly.

The inclusion of spin waves in the model requires an extension of the basic X-Y-Z coordinate system defined in Fig. 1. The two important extensions are depicted by the diagrams in Fig. 4. First, it is useful to introduce an additional reference frame as defined in Fig. 4(a). Here, in addition to the sample or laboratory X-Y-Z frame, one considers an x-y-z frame of reference in which the static component of the magnetization $\mathbf{M}_s$ is directed along the z axis. For the present purposes, this z axis is taken to lie in the Y-Z plane of the sample reference frame and is at an angle ϕ relative to the Z axis. Recall that ϕ is the angle between the $\mathbf{M}_s$ and the film normal. With $\mathbf{M}_s$ along the z axis, the precession of the full magnetization vector $\mathbf{M}$ yields a dynamic magnetization $\mathbf{m}$ which, to first order, only has x and y components. Hence, the x-y-z frame may be termed the ''precessional'' frame. This frame, as depicted in Fig. 4(a), has the x axis along X and the y axis in the Y-Z plane and rotated away from the Y axis by the angle ϕ. Note that for a static magnetization angle $\phi=0°$, the x-y-z frame is equivalent to the X-Y-Z frame. For other orientations, the x-y-z frame is obtained by a clockwise rotation of the X-Y-Z frame about the X axis by an angle ϕ.

One may now establish parameters to define the spin wave wave vector $\mathbf{k}$. A suitable definition for these parameters may be based on (b) of Fig. 4. The wave vector is specified in terms of a magnitude k, a polar angle θ_k, which is measured relative to the z axis, and an azimuthal angle ϕ_k, which corresponds to the angle between the projection of $\mathbf{k}$ on the x-y plane and the x axis.

In order to determine the spin wave dispersion relations from Eq. (11), the dynamic magnetization associated with a given spin wave is written in the form of a plane wave with a wave vector $\mathbf{k}$ and frequency ω_k

$$\mathbf{m}(\mathbf{r},t)=\mathbf{m}_k e^{-i(\mathbf{k}\cdot\mathbf{r}-\omega_k t)}. \tag{12}$$

The two components of the vector $\mathbf{m}_k$ are the complex x and y amplitudes of the spin wave and $\mathbf{r}$ denotes a general space coordinate. The magnetic field $\mathbf{H}(\mathbf{r},t)$ consists of a number of terms which may be written as

$$\mathbf{H}(\mathbf{r},t)=H_i\mathbf{z}+\mathbf{h}_{\text{an}}(\mathbf{r},t)+\mathbf{h}_{\text{dip}}(\mathbf{r},t)+\mathbf{h}_{\text{exch}}(\mathbf{r},t). \tag{13}$$

Here, H_i is an effective internal static magnetic field and the three additional fields denoted by lower case $\mathbf{h}$ are dynamic fields associated with the spin wave dynamic magnetization of Eq. (12). The first dynamic field, $\mathbf{h}_{\text{an}}(\mathbf{r},t)$, is associated with the crystalline anisotropy, the field $\mathbf{h}_{\text{dip}}(\mathbf{r},t)$ is the spin wave dipole field, and $\mathbf{h}_{\text{exch}}(\mathbf{r},t)$ is an effective exchange field for the spin wave.

The various terms in the effective field expression of Eq. (13) have been developed in the literature in various formats. The basic approach is given in Ref. 23, among others. It is assumed that the static equilibrium condition of Eq. (1) is satisfied. This means that the static effective field is parallel to the static magnetization vector, and hence, along the z axis. The static field term H_i may be written as

$$H_i=H_{\text{ext}}\cos(\theta-\phi)-2\pi M_s[\sin^2\phi+N_Z(3\cos^2\phi-1)]+H_A\cos^2\phi. \tag{14}$$

The first term on the right side of Eq. (14) is simply the component of the static external field along the direction of the static magnetization vector. The second term is the contribution from the static demagnetization field. The third term in Eq. (14) is the contribution to the static effective field due to the uniaxial anisotropy. It is important to emphasize that this term does not represent a real magnetic field in the Maxwellian sense. It is an effective field based on the specific form taken for the anisotropy energy. If a different form for $E_K(\phi)$ was used, $E_K=+K_U\sin^2\phi$, for example, this last term in Eq. (14) would change, as would Eq. (15) for the dynamic anisotropy field $\mathbf{h}_{\text{an}}$.

The next term in Eq. (13) is the effective dynamic anisotropy field $\mathbf{h}_{\text{an}}(\mathbf{r},t)$. This term is needed to account for the dynamic effects of the uniaxial anisotropy associated with the dynamic magnetization. For anisotropy as defined above, the dynamic effective anisotropy field is given by

$$\mathbf{h}_{\text{an}}(\mathbf{r},t)=\frac{H_A\mathbf{m}_k\cdot\mathbf{y}}{M_S}(\mathbf{y}\sin^2\phi-\mathbf{z}\sin\phi\cos\phi)\times e^{-i(\mathbf{k}\cdot\mathbf{r}-\omega_k t)}. \tag{15}$$

This effective anisotropy field is specified in the x-y-z frame. Procedures to obtain such effective fields are discussed in Ref. 23.

The next field, $\mathbf{h}_{\text{dip}}(\mathbf{r},t)$, accounts for the dipole–dipole interaction due to the misalignment of nearby spins associated with the plane wave excitation of Eq. (12). For the case of the uniform precession, where $\mathbf{k}=0$, there is no such dipole field because all of the spins are parallel. The dipole field can be conveniently expressed in terms of the wave vector and the dynamic magnetization for the spin wave according to

$$\mathbf{h}_{\text{dip}}(\mathbf{r},t)=-\frac{4\pi}{k^2}\,\mathbf{k}[\mathbf{k}\cdot\mathbf{m}_k]e^{-i(\mathbf{k}\cdot\mathbf{r}-\omega_k t)}. \tag{16}$$

The dipole field given in Eq. (16) is valid in the so-called magnetostatic approximation in which the wave number k for a given frequency is much greater than the corresponding pure electromagnetic wave wave number. These considerations are discussed in Ref. 37.

The last field term in Eq. (13) is the effective exchange field $\mathbf{h}_{\text{exch}}(\mathbf{r},t)$. This field, like the static and dynamic anisotropy fields, is not a true Maxwellian field, but is needed in order to account for the quantum mechanical exchange interaction. For a ferromagnetic material, this field can be written as

$$\mathbf{h}_{\text{exch}}(\mathbf{r},t)=-\frac{D}{M_s}\,k^2\mathbf{m}_k e^{-i(\mathbf{k}\cdot\mathbf{r}-\omega_k t)}. \tag{17}$$

The form of this exchange field is discussed in Ref. 3, among others. The D parameter characterizes the strength of the exchange. For ferrite materials, D has a nominal value in the 5×10^{-9} Oe cm^2/rad^2 range. This value will be used for the explicit numerical results presented below. It is assumed that D is independent of $\mathbf{k}$. Note that for the hexagonal ferrite materials, D may actually show a strong dependence on propagation direction.[11,21] Such effects have not been included in the present analysis.

In order to obtain dispersion relations of frequency ω_k as a function of $\mathbf{k}$, the torque equation of Eq. (11), together with the above effective field equations, are first linearized in the x and y components of the dynamic magnetization $\mathbf{m}_k$, taken as m_{kx} and m_{ky}, respectively. One then obtains a set of two homogeneous equations in m_{kx} and m_{ky}. The secular determinant from these equations leads to an expression for the spin wave frequency ω_k as a function of the wave vector $\mathbf{k}$. The general spin wave dispersion relation for a uniaxial or planar anisotropy material is obtained as

$$\begin{aligned}\omega_k^2=\gamma^2(H_i+Dk^2)(H_i+Dk^2+4\pi M_s\,\sin^2\,\theta_k-H_A\,\sin^2\,\phi)\\ -\gamma^2 4\pi M_S H_A\,\sin^2\,\phi\,\sin^2\,\theta_k\,\cos^2\,\phi_k.\end{aligned} \tag{18}$$

The validity of this dispersion relation is contingent upon the satisfaction of the stability condition of Eq. (1), as well as the other conditions specified above.

Equation (18) gives the general form of the bulk spin wave dispersion relation for a uniaxially anisotropic material magnetized at any angle ϕ relative to the crystalline c axis in the magnetostatic approximation. If the anisotropy field H_A is set to zero, this equation reduces to the well known dispersion relation for an isotropic ferrite material

$$\omega_k^2=\gamma^2(H_i+Dk^2)(H_i+Dk^2+4\pi M_s\,\sin^2\,\theta_k). \tag{19}$$

For the case of a uniaxial material with the external field in the c plane, such that $\phi=90°$ is satisfied, Eq. (18) reduces to the hexagonal ferrite dispersion relation of Joseph, Schlömann, and Bady.[21]

Two other special cases of the spin wave dispersion relation will be useful for the two magnon calculations. The first is the dispersion relation corresponding to propagation along the internal field and static magnetization directions, such that $\theta_k=0$ is satisfied. This represents the lowest possible spin wave frequency. This frequency is denoted as ω_{min} and is given by

$$\omega_{\text{min}}^2=\gamma^2(H_i+Dk^2)(H_i+Dk^2-H_A\,\sin^2\,\phi). \tag{20}$$

The second special dispersion relation is for propagation perpendicular to the static magnetization direction at $\theta_k=90°$. This frequency, denoted as ω_{max}, corresponds to the top of the spin wave band

$$\begin{aligned}\omega_{\text{max}}^2=\gamma^2(H_i+Dk^2)(H_i+Dk^2-H_A\,\sin^2\,\phi)\\ +\gamma^2 4\pi M_s(H_i+Dk^2-H_A\,\sin^2\,\phi\,\cos^2\,\phi_k).\end{aligned} \tag{21}$$

Note that ω_{max} depends on the azimuthal spin wave propagation angle ϕ_k, while ω_{min} does not depend on this angle.

It is clear from Eqs. (14) and (18) that the spin wave dispersion will depend strongly on the orientation of the static field and magnetization vectors. As shown in Fig. 2, this field value can vary over a wide range as the orientation angle θ of the external field is varied over the entire range of values from 0° to 90°. In the case of an isotropic material, the effect of this field variation is to shift the spin wave dispersion frequency band, relative to the FMR frequency, as θ is changed. For anisotropic materials, the effect is much more involved. The spin wave dispersion curves are not only shifted, but change in shape as well.

B. Spin wave dispersion and two magnon scattering

It is instructive to consider representative spin wave dispersion band diagrams for the three material cases introduced above. Such diagrams for YIG, Ba–M, and Zn–Y materials are shown in Figs. 5–7, respectively. In each case, band diagrams are shown for a range of external field orientations from out-of-plane at $\theta=0°$ to in-plane at $\theta=90°$. For each diagram in a given figure, the value of the internal field H_i was adjusted to produce the FMR peak response at a particular fixed FMR frequency and a range of illustrative external field orientations. Figure 5 for YIG shows the band diagram in the usual two dimensional format of spin wave frequency ω_k versus wave number k. Figures 6 and 7 for Ba–M and Zn–Y show both two dimensional and three dimensional plots.

Consider the diagrams in Fig. 5 for an isotropic thin YIG film and an FMR frequency of 10 GHz. The values of H_{ext} needed to obtain the diagrams in Fig. 5 are the same as the H_{FMR} values in Fig. 2 (a). Figure 2(a) is for the field applied out of the plane at $\theta=0°$, 2(b) is for $\theta=45°$, and 2(c) is for $\theta=90°$. In each case, two specific dispersion branches of spin wave frequency ω_k versus wave number k are shown.

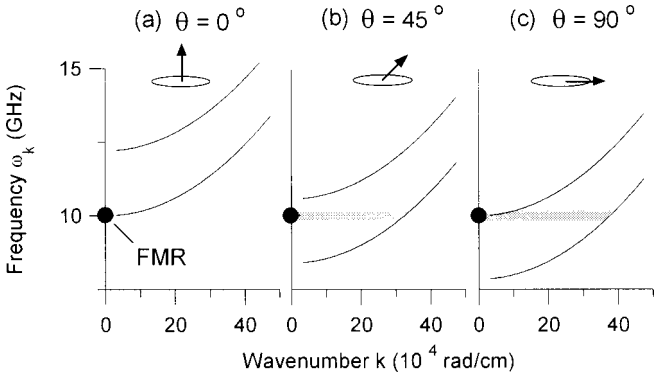

FIG. 5. Diagrams showing bulk spin wave dispersion curves of spin wave frequency ω_k vs wave number k for a thin YIG film and three orientations of the external static field, with the sample biased at the static field needed for FMR at 10 GHz. The lower curve in each diagram designates spin waves propagating parallel to the static internal field direction and the upper curve is for spin waves propagating perpendicular to the internal field direction. The region between the two curves represents the range of spin waves between these limiting case propagation directions. For (a) the static field is applied perpendicular to the film plane at $\theta=0°$. For (b) the static field is applied at $\theta=45°$. For (c) the static field is applied in the film plane at $\theta=90°$. The FMR frequency is indicated by the large solid circles. In (b) and (c), the narrow band of spin wave modes, which is degenerate with the FMR frequency, is indicated by the shaded region.

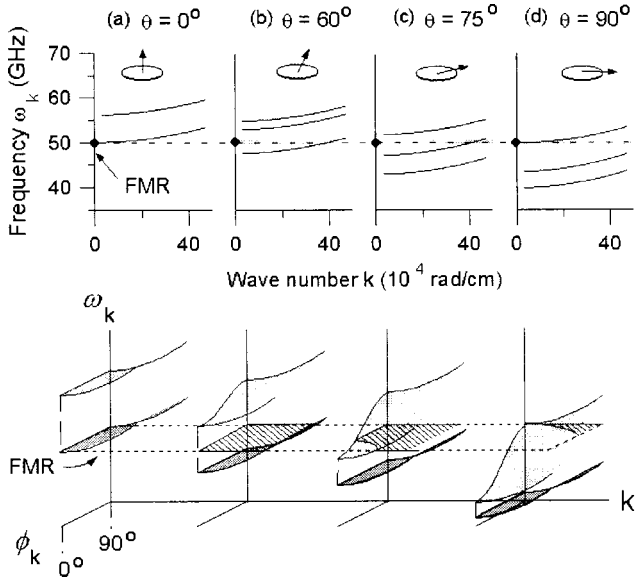

FIG. 6. Bulk spin wave dispersion diagrams for a thin Ba–M film and four orientations of the external static field, with the sample biased at the static field needed for FMR at 50 GHz. The top part of each set of diagrams shows calculated dispersion curves in the usual spin wave frequency ω_k vs wave number k format used in Fig. 5. For the upper diagrams, the top curves in (a) and the top pair of curves in (b), (c), and (d) correspond to a polar spin wave angle θ_k of 90°, and the bottom curves in (a)–(d) correspond to $\theta_k=0°$. The horizontal dashed line in (a) and the hatched line in (b)–(d) indicates the FMR frequency. The bottom part of each set shows schematic illustrations of the spin wave bands in three dimensions, with the azimuthal spin wave propagation angle ϕ_k out of the page. For these lower diagrams, the top shaded surface corresponds to $\theta_k=90°$ and the bottom shaded surface is for $\theta_k=0°$. The middle horizontal plane, which crosses all the diagrams, indicates the FMR frequency. For diagram set (a) the static field is applied perpendicular to the film plane at $\theta=0°$. For set (b) the static field is applied at $\theta=60°$. For set (c) the static field is applied at $\theta=75°$. For set (d) the static field is applied in the film plane at $\theta=90°$.

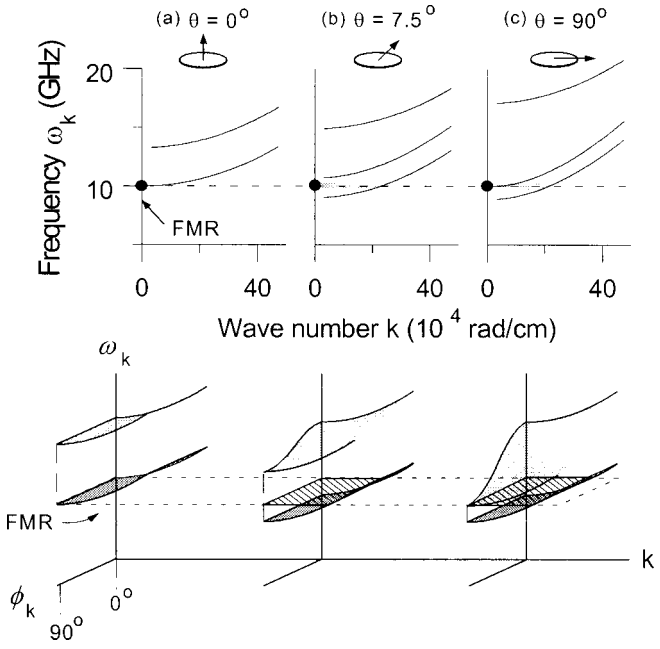

FIG. 7. Bulk spin wave dispersion diagrams for a thin Zn–Y film and three orientations of the external static field, with the sample biased at the static field needed for FMR at 10 GHz. The top part of each set of diagrams shows calculated dispersion curves in the usual spin wave frequency ω_k vs wave number k format used in Fig. 5. For the upper diagrams, the top curves in (a) and the top pair of curves in (b) and (c) correspond to a polar spin wave angle θ_k of 90°, and the bottom curves in (a)–(c) correspond to $\theta_k=0°$. The horizontal dashed line in (a) and the hybrid dashed-hatched line in (b)–(c) indicate the FMR frequency. The bottom part of each set shows schematic illustrations of the spin wave band in three dimensions with the azimuthal spin wave propagation angle out of the page. Note that the orientation of the ϕ_k axis is reversed from the ϕ_k axis in Fig. 6. For these lower diagrams, the top shaded surface corresponds to $\theta_k=90°$ and the bottom shaded surface is for $\theta_k=0°$. The middle horizontal plane which crosses all the diagrams indicates the FMR frequency. For diagram set (a), the static field is applied perpendicular to the film plane at $\theta=0°$. For set (b), the static field is applied at $\theta=7.5°$. For set (c), the static field is applied at $\theta=90°$.

The lower curve corresponds to spin waves at $\theta_k=0°$, or propagation parallel to the static magnetization direction, as specified by Eq. (19) or by the frequency $\omega_{\min}$ of Eq. (20) for $H_A=0$. The upper curve corresponds to spin waves at $\theta_k=90°$, or propagation perpendicular to the static magnetization direction, as specified by Eq. (19) or by the frequency $\omega_{\max}$ of Eq. (21) for $H_A=0$. The band of available spin waves consists of the regions between these lower and upper curves. The FMR frequency is indicated in each diagram by the solid circle. The horizontal shaded strips in (b) and (c) indicate the range of spin waves which are degenerate with the FMR frequency. These states will be important for the two magnon scattering interaction.

The important result in Fig. 5 for two magnon scattering is the shift of the band as the external field orientation is rotated from perpendicular to parallel. In the perpendicular configuration of (a), the bottom of the spin wave band at $k=0$ is coincident with the FMR frequency and there are no nonzero k spin wave states at this frequency. In the parallel configuration of (c), the band has dropped down so that the top of the spin wave band at $k=0$ is coincident with the FMR frequency. There is now an extended range of spin wave states degenerate with the FMR frequency. These

states range from spin waves at $k=0$ for $\theta_k=90°$ to rather large k values at $\theta_k=0°$. Note that the maximum value of k for degenerate states is in the range $3-4\times10^5$ rad/cm, or wavelengths in the 0.2 μm range.

The shift in the frequency of the spin wave band relative to the YIG film FMR frequency as H_{ext} is rotated from $\theta=0°$ to $\theta=90°$ is due to two effects. First, it is evident from Fig. 2(a) that the external field required for ferromagnetic resonance at 10 GHz, H_{FMR}, is much larger at $\theta=0°$ than at $\theta=90°$. From the results in Fig. 2(a), H_{FMR} drops from over 5 kOe for $\theta=0°$ to less than 1 kOe for $\theta=90°$. The corresponding internal field H_i also drops as the static field is rotated from perpendicular to parallel. Second, the changing role of the static and dynamic demagnetizing fields works to position the thin film FMR frequency precisely at the bottom of the $k=0$ spin wave band limit at $\theta=0°$ and precisely at the top of the $k=0$ band limit for $\theta=90°$.

The net effect of these FMR and spin wave band shifts is a variation in the availability of spin wave states at the FMR frequency with angle. Since these are the spin wave states which can contribute to two magnon scattering relaxation, one is able to vary this contribution to the overall relaxation simply by rotating the direction of the static field used to produce the FMR response. If two magnon processes are important, the profile of FMR linewidth ΔH versus the field angle θ at fixed frequency will be different from the constant $1/T$ profiles shown in Fig. 3. These differences can provide a signature profile for the two magnon scattering process.

Turn now to the dispersion relations for anisotropic Ba–M and Zn–Y films. As made explicit in Eqs. (18), (20), and (21), the spin wave frequencies in these materials depend, in general, on the azimuthal spin wave propagation angle ϕ_k as well as the polar angle θ_k and the wave number k. It is now necessary to include ϕ_k as a parameter when dispersion curves are computed. Examples of the anisotropic spin wave band for the case of a Ba–M film and an FMR frequency of 50 GHz are shown in Fig. 6. The upper diagrams show calculated curves in the two dimensional ω_k vs k format of Fig. 5. The lower diagrams show three dimensional plots of ω_k as a function of k and ϕ_k. Figure 5(a) is for $\theta=0°$. Figures 5(b) and 5(c) are for $\theta=60°$ and $\theta=75°$, respectively. Figure 5(d) is for $\theta=90°$. Note the ϕ_k axis scale in the lower set of diagrams, which was chosen to provide the best perspective view of the spin wave band.

The curves in the upper diagrams and the two shaded curved surfaces in the lower diagrams correspond to different (θ_k,ϕ_k) combinations. The bottom curved surfaces in the lower diagrams are for $\theta_k=0°$ and the upper curved surfaces are for $\theta_k=90°$. Corresponding projections of the edge curves for $\phi_k=0°$ and $\phi_k=90°$ from the bottom diagrams yield the curves shown in the upper diagrams. The bottom curves in the upper diagrams, for example, are all for $\theta_k=90°$ and do not depend on ϕ_k. The other projections are clear from the diagrams. The main effect of the anisotropy is to produce spin wave frequency surfaces as a function of k and ϕ_k for fixed values of θ_k. When the applied field is such that the rotational symmetry is broken, e.g., when θ is any angle except zero and θ_k is also any angle except zero, the θ_k surface is warped. The warp is most pronounced at $\theta=90°$ and $\theta_k=90°$.

Turn now to the FMR response. The dashed line in the upper diagrams and the horizontal plane in the lower diagrams, both labeled as FMR, indicate the FMR frequency of 50 GHz which is common to all the diagrams. This FMR frequency is the same as for Fig. 2(b). The shaded strip in the upper diagrams and the shaded part of the FMR plane in the lower diagrams indicate the range of spin wave modes with ω_k the same as the FMR frequency.

The basic effect conveyed by the diagrams in Fig. 6 for the c plane Ba–M film is the same as for the isotropic YIG film. As one moves from the perpendicular FMR configuration at $\theta=0°$ to the parallel FMR case at $\theta=90°$, with the external field adjusted to keep the FMR frequency constant, the spin wave band of frequencies shifts relative to the FMR frequency and there is a substantial change in the spin wave states which are degenerate at this frequency. The situation at $\theta=0°$ shown in the left-most diagrams in Fig. 6, is the same as for the YIG case: no degenerate spin wave states except at $k=0$. Now, as θ is increased from zero, the entire band moves down in frequency and various spin wave states move into the FMR frequency strip in the upper diagrams or FMR frequency cut in the lower diagrams of Fig. 6.

The situation here, however, is more complicated than for YIG. In order to understand the evolution of the degenerate spin wave states with angle θ, it is necessary to follow in detail the change in the shaded part of the FMR frequency cut in the lower diagrams in Fig. 6. Consider the lower part of (b), for example. As long as θ is not increased too much, the FMR frequency cut extends across the spin wave band in such a way that there are degenerate states for all values of all ϕ_k from 0° to 90° and k values from zero out to some mzximum cut-off defined by the $\theta_k=0°$ edge of the band. This range of degenerate spin wave states is indicated by the shaded part of the FMR frequency cut in the lower part of Fig. 6(b) for $\theta=60°$ and the shaded strip in the upper part. The situation changes as one moves to $\theta=75°$ and Fig. 6(c). Now, as shown by the shaded part of the FMR frequency cut in the lower diagram of the set, the available degenerate spin waves become more limited. Here, for small values of k, the allowed ϕ_k values for degenerate spin waves range from some lower ϕ_k limit up to $\phi_k=90°$. This lower ϕ_k limit increases and approaches 90° as one moves up to an external field angle $\theta=90°$ and a parallel FMR configuration. This degenerate spin wave situation is indicated by the very small shaded section of the FMR frequency cut for the lower part in Fig. 6(d). The details of these changes in the available degenerate spin wave states as θ is varied will have important consequences for two magnon scattering.

Figure 7 shows the evolution in the spin wave band with the external field angle θ for Zn–Y and an FMR frequency of 10 GHz. The format is the same as for the Ba–M diagram in Fig. 6 and will not be described in detail. There are several important differences between the Zn–Y and Ba–M diagrams. The Zn–Y film represents an easy-plane rather than an easy-axis situation. The first effect of this change in anisotropy is that the warped spin wave band surfaces are reversed. Although the warped surfaces look the same in Fig. 7

as in Fig. 6, note that the ϕ_k axes are reversed. The second effect is in the movement in the band relative to the FMR frequency as the field angle θ is changed. For the perpendicular configuration and $\theta=0°$, the FMR frequency point is located at the very bottom of the band, as before. For the parallel configuration and $\theta=90°$, however, the FMR frequency point is at the bottom of the warped $\theta_k=90°$ spin wave surface at $k=0$, rather than at the top of this surface. There are never any excluded ϕ_k modes from the two magnon scattering process. As the field angle θ is rotated from 0° to 90°, the spin wave band moves only part way down and there is no drastic change in the degenerate state situation as for Ba–M. One would expect that the two magnon linewidth profile for Zn–Y would be much simpler than for either Ba–M or for YIG films.

IV. TWO MAGNON SCATTERING THEORY

The two magnon relaxation rate corresponds to the rate at which energy is transferred from the uniform precession to degenerate spin waves due to the presence of magnetic inhomogeneities. It is assumed that these excited spin waves then relax to the lattice extremely rapidly and do not affect the two magnon decay. The basic formalism has been taken over from the analysis developed by SLK.[4] This section is divided into three parts. The first part takes the SLK scattering relaxation rate as a starting point, and introduces several modifications which make the analysis more practical and applicable. The second part provides a detailed and specific development of the scattering integrals and limits which must be invoked to perform practical two magnon scattering calculations. The third part presents a qualitative and diagrammatic discussion of these spin wave regimes which contribute to the scattering.

A. A modified SLK two magnon scattering model

For a scattering inhomogeneity of a given size, the SLK model predicts the rate at which energy is coupled from the uniform precession of the magnetization vector over the entire sample, which is excited through the FMR response, to a particular spin wave due to the dipolar interaction between the scatterer and the spin wave. The net relaxation rate is then found from adding up the rates for all degenerate spin wave states for all of the scatterers in the sample. In the original SLK treatment, the scattering inhomogeneity was modeled as a spherical void in an infinite sample. The assumption of spherical symmetry leads to a **k**-dependent coupling between the uniform precession and the degenerate spin waves. That is, spin waves which propagate in certain directions and at certain k values couple more strongly to the uniform mode than others. This **k** dependence is due to the geometry of the dipole fields associated with the void. The SLK treatment then applied this result for a single spherical void to a sample with many identical scatterers by assuming that these scatterers operate independently.

One problem in the SLK formalism is that **k**-dependent scattering is associated directly with the spherical nature of the void used for the analysis. Modifications were also introduced to account for the expected occurrence of many nonspherical scatterers. Nonspherical scatterers were included through the addition of an *ad hoc* constant term to the **k**-dependent scattering factor in the coupling function.[19] Further comments on this modification will be given below. The SLK calculation has also been applied to the case of an obliquely magnetized thin film,[18] but the analysis was restricted to isotropic materials and spherical void scattering.

It is important to establish a clear connection between the relaxation rate obtained from the SLK approach and the linewidths which are obtained in the experiment. For a given two magnon relaxation rate $1/T_{\rm TM}$, the FMR frequency linewidth is simply $\Delta(\omega/\gamma)=1/\gamma T_{\rm TM}$. Once the frequency linewidth is determined, the field linewidth ΔH for two magnon scattering can be found from Eq. (10). It should be noted that many treatments specify the relaxation time τ_m associated with the decay of the dynamic magnetization amplitude rather than the decay of the energy associated with the dynamic magnetization. In that case, the frequency linewidth is given by $\Delta(\omega/\gamma)=2/\gamma\tau_m$.[38] The presentation here will use energy decay as the basic decay rate.

Several modifications have been made to the SLK approach. First, in order to deal with anisotropic films, the SLK treatment has been extended to account for the effects of anisotropy on both the FMR response and the spin wave dispersion properties. Second, the scattering calculation has been modified to include scattering into a band of nearly degenerate spin waves with a frequency width which corresponds to an average frequency linewidth for the scattered spin waves. This allows the subsequent relaxation of these scattered spin waves to be included in the analysis in a simple and intuitive manner. Third, specific calculations of angle dependent linewidths have been made for two limits: (i) a ''spherical void scattering'' limit in which the **k**-dependent scattering factor from the SLK model is assumed to apply and (ii) an ''isotropic scattering'' limit in which this scattering factor is assumed to be **k**-independent and equal to its average value over all angles. It is clear that purely spherical voids represent a poor approximation to the inhomogeneities in real materials. One would expect that these two limits would bracket the real physical situation for ferrite films with various microstructure properties.

The main result of the SLK theory is an expression for the relaxation rate due to a single scatterer. This rate is determined from a Fermi golden rule calculation and can be written as

$$\frac{1}{T_{\rm SLK}}=\frac{2\pi}{\hbar}\sum_{\mathbf{k}\neq 0}[F(\mathbf{k})]^2\,\delta(\hbar\omega_k-\hbar\omega). \tag{22}$$

Here, $\hbar$ is Planck's constant, $\delta(\hbar\omega_k-\hbar\omega)$ is the Dirac delta function, and the $[F(\mathbf{k})]^2$ factor represents the coupling between the spherical void and the degenerate spin waves. The sum spans the various **k** values in the spin wave band, but with the uniform mode excluded.

The $F(\mathbf{k})$ coupling factor is given by

$$F(\mathbf{k})=16\pi^2 M_s R^3\,\frac{\mu}{V}\,(3\cos^2\,\theta_k-1)\,\frac{j_i(kR)}{kR}. \tag{23}$$

Here, R is the scatterer radius, μ is the Bohr magneton, V is the sample volume, and $j_1(kR)$ is the first spherical Bessel

function. In addition to the development in the original SLK paper, a detailed derivation of Eqs. (22) and (23) is given by Haas and Callen.[39] It is useful to note that γ, the magnitude of the electron gyromagnetic ratio, is given by $\gamma=2\mu/\hbar$. The matter of units will be considered shortly.

Equations (22) and (23) are the key working equations for two magnon scattering calculations. The net relaxation rate is in the form of a sum over all k states. The sum is weighted by the Dirac delta function. This insures that only degenerate spin waves, that is, spin waves with $\omega_k=\omega$, are included in the summation. Each relaxation rate sum term is proportional to $[F(\mathbf{k})]^2$, which is related to the interaction energy between the uniform mode and the spin wave at wave vector $\mathbf{k}$.

In practice, the Dirac delta function in Eq. (22) should be replaced by a function of finite width in order to account for the subsequent relaxation of the degenerate spin waves. One simple approximation to the delta function which has finite width and unit area is

$$G(\omega,\omega_k)=\begin{cases}\dfrac{1}{\hbar\Delta\omega_i}, & \omega-\dfrac{\Delta\omega_i}{2}<\omega_k<\omega+\dfrac{\Delta\omega_i}{2}\\ 0, \quad \text{otherwise.}\end{cases} \tag{24}$$

Here, $\Delta\omega_i$ is the intrinsic frequency linewidth which characterizes the magnetic loss for the material in the absence of two magnon scattering. This linewidth is taken to be an order of magnitude estimate to describe the intrinsic relaxation of the degenerate spin waves.

Turn now to the $[F(\mathbf{k})]^2$ term. Note that $[F(\mathbf{k})]^2$ varies as M_s^2. This dependence on the square of the magnetization reflects the dipole–dipole origin of the two magnon scattering interaction. The specific form of the $(3\cos^2\theta_k-1)^2$ term is due to the assumption of spherically shaped scatterers. Because of the spatial dependence of the dipole field associated with the spherical void, spin waves which propagate in certain directions couple more strongly to the scatterer than others. For a spin wave propagating parallel to the static magnetization direction, at $\theta_k=0$, $(3\cos^2\theta_k-1)^2$ is equal to 4. For a spin wave propagating perpendicular to the z axis at $\theta_k=90°$, $(3\cos^2\theta_k-1)^2$ is equal to 1. For $\cos^2\theta_k=1/3$, or $\theta_k=54.7°$, this angular coupling function is equal to zero. Spin waves at this propagation angle do not participate in the two magnon process at all. The use of the $(3\cos^2\theta_k-1)^2$ term will be identified as ''spherical void scattering.''

The vanishing of the two magnon coupling at $\theta_k=54.7°$ for spherical void scattering is related to properties of the dipole field around the void. If one considers a conical surface defined by all rays which extend away from the void at an angle of 54.7° relative to the saturation magnetization direction, the static dipole field along this surface is always perpendicular to the static magnetization. The dynamic dipole field associated with the uniform precession is, therefore, parallel to the direction of the static magnetization. The SLK analysis shows that this parallel dynamic field does not couple to spin waves propagating in the coincident direction at $\theta_k=54.7°$.

In addition to the assumption of spherical inhomogeneities and the corresponding $(3\cos^2\theta_k-1)^2$ coupling term, it will be useful to consider possible angle dependences for the case of nonspherical scatterers. In order to model the effect of nonspherical inhomogeneities, it is reasonable to replace $(3\cos^2\theta_k-1)^2$ with its average value over all solid angles of 0.8. This approach is designated ''isotropic scattering.''

It is important to note that Sparks,[18] Seiden and Sparks,[19] and Sage[20] have all proposed various modifications to the SLK model to account for nonspherical scatterers. In each case, the resultant angular coupling function included both spherical void and isotropic scattering terms. The present approach appears to be intuitively plausible and operationally convenient.

Consider now the role of the $[j_1(kR)/kr]^2$ term in the relaxation rate expression. This function has a value of 1/9 for $kR=0$ and is essentially zero for $kR>\pi$. This factor insures that the degenerate spin waves which participate in the two magnon process have wavelengths on the order of the scatterer size or larger. This means that for large inhomogeneities, only spin waves with low wave numbers can contribute. For smaller inhomogeneities, higher wave number spin waves can participate. For very small R values, degenerate spin waves with all available k values can contribute appreciably to the scattering. It will be seen that the size of the scattering inhomogeneities will have a significant effect on the shape of the linewidth versus field angle profile.

For simplicity, and following the SLK approach, it is assumed that the material contains N independent, identical scatterers of radius R. The net linewidth is then given by Eq. (22) multiplied by a factor of N.

B. Two magnon scattering integrals and limits

In order to evaluate the two magnon relaxation rates, it is useful to convert the sum over $\mathbf{k}$ states to an integration over k space. The sum in Eq. (22) is replaced by an integral.

$$\sum_{\mathbf{k}} \rightarrow \frac{V}{8\pi^3}\int\int\int d^3\mathbf{k}. \tag{25}$$

The factor $V/8\pi^3$ represents the number of states per unit volume in k space. The two magnon relaxation rate $1/T_{\mathrm{TM}}$ for N scatterers is given by

$$\frac{1}{T_{\mathrm{TM}}}=\frac{NV}{4\pi^2\hbar}\int_0^{\infty}\int_0^{2\pi}\int_0^{\pi}[F(\mathbf{k})]^2G(\omega,\omega_k) \times k^2\sin\theta_k d\theta_k d\phi_k dk. \tag{26}$$

It is more useful, however, to cast Eq. (26) in a form for which the integration limits directly reflect the spin wave band and range of degenerate states. To do so, it is necessary to eliminate the $G(\omega,\omega_k)$ function in the integrand. Since $G(\omega,\omega_k)$ is equal to $1/\hbar\Delta\omega_i$ for degenerate spin waves but is zero otherwise, this function can be replaced by $1/\hbar\Delta\omega_i$ if the integration limits are modified appropriately. The first integration, over the $\cos\theta_k$ variable, reflects the range of θ_k values for the degenerate spin waves for a given k and ϕ_k. The second integration is over ϕ_k. For an isotropic material, this integration is trivial because the spin wave dispersion relations show no dependence on the ϕ_k. For a uniaxial material, the ϕ_k dependence can play a significant role and

may result in a modification to the integration limits as well. The third integration is over the wave number k.

In terms of the new integration limits, the two magnon relaxation rate may be written as

$$\frac{1}{T_{\mathrm{TM}}}=\frac{6p\gamma^2(4\pi M_s)^2R^3}{\pi\Delta\omega_i}\times\int_0^{\infty}\int_{f(k)}^{\pi/2}\int_{a(k,\phi_k)}^{b(k,\phi_k)}\left((3\cos^2\theta_k-1)\frac{j_i(kR)}{kR}\right)^2\times d(\cos\theta_k)d\phi_k k^2\,dk. \tag{27}$$

Here, p is the ratio of total scatterer volume to the sample volume, $4\pi R^3/3V$. The condition $\gamma=2\mu/\hbar$ has been invoked to eliminate μ and $\hbar$ from the relaxation rate expression. In the format of Eq. (27), the various units are clear. Both $\gamma 4\pi M_s$ and $\Delta\omega_i$ have units of rad/s, so that $1/T_{\mathrm{TM}}$ also has units of rad/s.

The $a(k,\phi_k)$ and $b(k,\phi_k)$ limit functions for the $\cos\theta_k$ integral are derived from the anisotropic spin wave dispersion relation of Eq. (18). The $a(k,\phi_k)$ and $a(k,\phi_k)$ functions give the value of $\cos\theta_k$ when the spin wave frequency ω_k is at the top or bottom of the finite width band of nearly degenerate states, respectively, or at $\omega_k=\omega\pm\Delta\omega_i/2$. These functions may be written as

$$\begin{matrix}a(k,\phi_k)\\ b(k,\phi_k)\end{matrix}=\begin{cases}1, & \omega\pm\dfrac{\Delta\omega_i}{2}<\omega_{\min}\\ \sqrt{\dfrac{\omega_{\max}^2-\left(\omega\pm\dfrac{\Delta\omega_i}{2}\right)^2}{\omega_{\max}^2-\omega_{\min}^2}}, & \omega_{\min}<\omega\pm\dfrac{\Delta\omega_i}{2}<\omega_{\max}\\ 0, & \omega\pm\dfrac{\Delta\omega_i}{2}>\omega_{\max}\end{cases} \tag{28}$$

The $\pm$ signs apply to $a(k,\phi_k)$ and $a(k,\phi_k)$, respectively. The frequencies $\omega_{\min}$ and $\omega_{\max}$ are the same as given by Eqs. (20) and (21). The limit values of zero and one for $a(k,\phi_k)$ and $b(k,\phi_k)$ apply when the wave number k is greater than the largest value of k allowed by the dispersion or when k is less than the smallest allowed value, respectively. When both limits are zero or one, of course, the integral will vanish.

The function $f(k)$ represents the minimum value of ϕ_k at $\omega_k=\omega$ for a given field orientation. This $f(k)$ may be written in implicit form through the condition

$$\cos^2[f(k)]=\frac{\gamma^2(H_i+Dk^2)(H_i+Dk^2-H_A\sin^2\phi+4\pi M_s)-\omega^2}{4\pi M_s\gamma^2H_A\sin^2\phi}. \tag{29}$$

Equation (29) is valid provided that the right hand side is positive and less than or equal to 1. Otherwise, the function $f(k)$ is simply zero. By this definition, $f(k)$ is zero for an isotropic material where $H_A=0$.

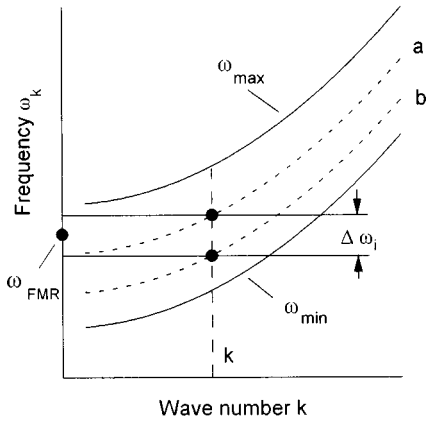

FIG. 8. Schematic illustration of the spin wave dispersion curves of spin wave frequency ω_k vs wave number k at some particular azimuthal spin wave angle ϕ_k, shown by the curved solid lines, and the band of allowed spin wave frequencies for two magnon scattering, shown by the horizontal solid lines. The bottom solid curve labeled $\omega_{\min}$ corresponds to $\theta_k=0°$. The top solid curve labeled $\omega_{\max}$ corresponds to $\theta_k=90°$. The scattering band defined by the solid horizontal lines is centered on the FMR frequency indicated as ω_{FMR} and has a width $\Delta\omega_i$. For a particular wave number k, as indicated by the vertical dashed line, and the selected azimuthal angle ϕ_k, the curves and the lines intersect at the solid circles as shown. The upper solid circle identifies the integration limit function $a(k,\phi_k)$ given in Eq. (28) and the value of $\cos\theta_k$ which matches the upper dashed dispersion curve labeled as a in the figure. The lower solid circle identifies the $b(k,\phi_k)$ integration limit function given in Eq. (29) and the value of $\cos\theta_k$ which matches the lower dashed dispersion curve labeled as b in the figure.

C. Discussion of two magnon scattering regimes

The $a(k,\phi_k)$, $b(k,\phi_k)$, and $f(k)$ limits can best be understood from graphical illustrations of the $\cos\theta_k$ and ϕ_k integrations. The $\cos\theta_k$ integration is placed in perspective in Fig. 8. The figure shows various spin wave dispersion curves of frequency ω_k as a function of wave number k, all for a given value and orientation of the external magnetic field and some specific azimuthal spin wave propagation angle ϕ_k. The format is the same as with the previous two dimensional spin wave band diagrams. The top and bottom dispersion branches are shown as solid curved lines labeled $\omega_{\min}$ and $\omega_{\max}$, respectively. These curves correspond to the dispersion curves for $\theta_k=90°$ and $\theta_k=0°$, as in previous diagrams. The point labeled ω_{FMR} denotes the FMR frequency and the operating frequency of interest. Given the orientation angle ϕ for the static external field, H_{ext}, the value of the field has been set to yield this FMR frequency.

The solid horizontal lines in Fig. 8 delineate the range of degenerate spin wave states which are within $1/2\Delta\omega_i$ of the operating frequency. This width has been exaggerated for the sake of illustration. For FMR frequencies in the GHz range, this degenerate band of states typically will have a width in the range of several tenths of a MHz to tens of MHz, depending on the intrinsic loss level of the ferrite film under consideration. The intersection of this horizontal band with the overall spin wave band from $\omega_{\min}$ to $\omega_{\max}$ gives the region of states in k and θ_k, for a given ϕ_k, which contribute to the two magnon scattering. In order to illustrate the $\cos\theta_k$ integration limits, the diagram shows a particular k value as indicated by the vertical dashed line. The intersections of this

line with the horizontal scattering band limits are indicated by the solid circles. The dashed curves through these two solid circles further identify spin wave dispersion curves at values of cos θ_k equal to a and b, as indicated. These a and b values correspond to the $a(k,\phi_k)$ and $b(k,\phi_k)$ integration limit functions introduced above.

It is straightforward to understand the cos θ_k integral in Eq. (27) from the diagram. This integral simply scans those states in θ_k along the vertical dashed line at constant k, from the a intersection point specified by cos $\theta_k = a(k,\phi_k)$, to the b intersection point specified by cos $\theta_k = b(k,\phi_k)$. If the chosen k or ϕ_k values are such that either or both intersection points fall below the solid $\omega_{\min}$ curve, one simply sets the corresponding cos θ_k limit to zero. If the chosen k or ϕ_k values are such that either or both intersection points fall above the solid $\omega_{\max}$ curve, one simply sets the corresponding cos θ_k limit to one. These assignments for $a(k,\phi_k)$ and $b(k,\phi_k)$ are expressed analytically through Eqs. (28) and (29).

It is clear from Fig. 8 that the $a(k,\phi_k)$ and $b(k,\phi_k)$ integration limits are related to the width $\Delta\omega_i$, while a $1/\Delta\omega_i$ dependence is present in the prefactor of Eq. (27). As long as $\Delta\omega_i \ll \omega$ is satisfied, the two magnon linewidth is essentially independent of $\Delta\omega_i$. It should also be noted that because there is another spin wave state at $\pi - \theta_k$ which is also degenerate, the introduction of the $a(k,\phi_k)$ and $b(k,\phi_k)$ limits is accompanied by an overall multiplication by a factor of 2.

Turn now to the azimuthal angle ϕ_k integration. Note that the integration in Eq. (26) was from 0 to 2π. By symmetry this integral can be evaluated over 0 to $\pi/2$ and then multiplied by a factor of 4. This factor of 4 is taken into account in Eq. (27). Equation (27) shows that, in addition, the lower limit on the ϕ_k integration is $f(k)$ rather than zero. As discussed above, the $f(k)$ function will be zero for isotropic materials with $H_A = 0$. For anisotropic materials, however, the distortion of the spin wave band and the additional dependences of the spin wave frequency on ϕ_k can lead to the exclusion of low ϕ_k states from the scattering integral. This effect is evident from the three dimensional dispersion diagram in (c) of Fig. 6 for the Ba–M film and $\theta = 75°$.

This same diagram is shown in Fig. 9(a). Figure 9(b) shows the same constant frequency cut as a graph of ϕ_k vs k. These graphs show that, under appropriate circumstances and for values of the wave number k below some upper limit value, the range of degenerate spin wave states is from some nonzero value of ϕ_k up to $\pi/2$. Under such circumstances, the $f(k)$ function of Eq. (30) gives this lower limit ϕ_k value. For the example of Fig. 9, the $f(k)$ function describes the curved lower left boundary for the shaded region of the graph in (b). Note that this lower ϕ_k limit is a function of the wave number k for low k but becomes zero at larger wave number. The point where this function becomes zero corresponds to the wave number for which the right hand side of Eq. (30) becomes zero. Note that the top ϕ_k limit is always 90°, independent of k.

It should also be noted that the $f(k)$ is nonzero only for the case of an easy-axis material magnetized near the out-of-plane direction. Figures 6(a) and 6(b) show no such ϕ_k cuts

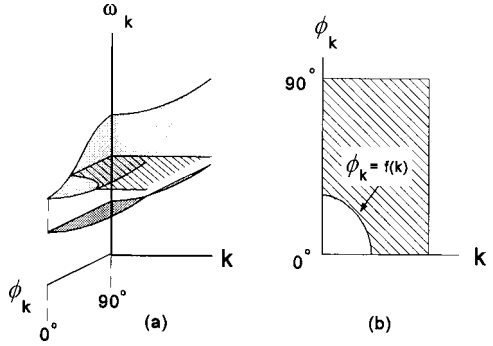

FIG. 9. Schematic illustration of the regime of degenerate spin wave states for a Ba–M sample magnetized in an oblique direction such that the FMR cut in Fig. 6 intersects the top $\theta_k = 90°$ surface. (a) shows the spin wave band in three dimensions, in the same format as in the lower diagram of set (c) in Fig. 6. As in Fig. 6, the thin band of degenerate spin wave states at the FMR frequency is indicated by the cross-hatched region. (b) shows this hatched region in a two dimensional plot of azimuthal spin wave angle ϕ_k vs wave number k. The function $f(k)$ for the lower limit of the ϕ_k integration in Eq. (27), defined mathematically through Eq. (30), is indicated by the curve labeled $\phi_k = f(k)$ in (b).

of the sort evident for (c) and (d). Moreover, for an easy-plane material such as Zn–Y, the $f(k)$ function is always zero, regardless of the field orientation. This result is evident from the three dimensional diagrams in Fig. 7. In these diagrams, the constant frequency cuts all include the full range of ϕ_k values.

Turn finally to the integration over wave number k. While the limits on the k integral are shown as zero to infinity, there is always an upper limit on k for which the line of degenerate states extends outside the spin wave band. This k cut-off is evident from all of the diagrams in Figs. 5–9. The explicit cut-off value of k, k_{cut}, is obtained from Eq. (20) for $\omega_{\min}$. One simply sets $\omega_{\min}$ in Eq. (20) equal to ω_{FMR} and solves for $k = k_{\text{cut}}$. Note that the two control parameters in Eq. (20), the internal static effective field H_i and the equilibrium static magnetization angle ϕ, are specified through H_{ext} and θ. The FMR frequency ω_{FMR} is also specified through H_{ext} and θ. In addition to this k state cut-off because of the spin wave band limits, there is also a practical cut-off through the $j_1(kR)$ function. The value of this spherical Bessel function in the integrand of Eqs. (26) and (27) is small for large values of kR. For practical purposes, $j_1(kR)$ can be set to zero for k values greater than π/R.

In closing this section, it is useful to enumerate the sequence of operations to calculate two magnon relaxation rates. (1) One first chooses the film material, the basic materials parameters γ, $4\pi M_s$, K_U and H_A, and an intrinsic frequency linewidth $\Delta\omega_i$. (2) One then chooses an operating frequency ω and solves (i) the static equilibrium problem and (ii) the FMR problem to obtain the FMR field, H_{FMR}, the internal field H_i, the static magnetization angle ϕ, and the value of k_{cut}, all as a function of the external field angle θ for all values of interest between 0° and 90°. (3) One then chooses inhomogeneity parameters R and p. (4) One then chooses either the ''spherical void scattering'' limit and incorporates the full $(3\cos^2\theta_k - 1)^2$ angle term in Eq. (27), or

selects the ''isotropic scattering'' limit in which this term is replaced by its average value of 0.8 over all solid angles.

One is now in a position to evaluate a two magnon relaxation rate $1/T_{TM}$ at these different values of ϕ, and hence, to obtain information on the two magnon frequency linewidth $1/\gamma T_{TM}$ or the corresponding field linewidth ΔH as a function of ϕ or θ. For each ϕ, this $1/T_{TM}$ is obtained from Eq. (27). For a given ϕ value, the first step is to determine the effective internal field H_i as given by Eq. (14). One can then write explicit expressions for $a(k,\phi_k)$ and $b(k,\phi_k)$ based on Eqs. (28), (20), and (21). In order to evaluate Eq. (27), the integral over cos θ_k should be performed first. This integration can be done analytically. The result is a complicated double integral over k and ϕ_k which can be handled by a number of numerical methods. One approach would be to use a quadrature algorithm for the ϕ_k integration nested within a second quadrature algorithm for the k integration.

V. EXPLICIT TWO MAGNON LINEWIDTH VERSUS ANGLE RESULTS

In this section, some representative two magnon results are presented. These are shown in terms of the frequency swept linewidth $\Delta(\omega/\gamma)$ and field swept linewidth ΔH versus the angle θ between the static magnetic field and the film normal. Various linewidth angle profiles for the YIG, Ba–M, and Zn–Y materials, different size voids, and different scattering limits are shown. These results will demonstrate the different types of linewidth angle profiles which can result from two magnon scattering.

Recall from Eq. (9) that the frequency linewidth $\Delta(\omega/\gamma)$ is simply proportional to the relaxation rate. This means that the angle dependences for $\Delta(\omega/\gamma)$ are identical to those for $1/T$. The only difference is that $\Delta(\omega/\gamma)$ conveniently expresses the calculated losses in terms of magnetic field units which correspond to linewidths. Recall as well that the field swept resonance linewidth ΔH can have significant angle dependences even for a constant $1/T$ or, therefore, a constant $\Delta(\omega/\gamma)$. For YIG films and frequencies in the 10 GHz range and above, the $\Delta(\omega/\gamma)$ and ΔH profiles are almost the same. This is due to the relatively small saturation induction and the nearly parallel alignment of $\mathbf{H}_{ext}$ and $\mathbf{M}_s$ as the field is rotated from out-of-plane to in-plane and $\mathbf{H}_{ext}$ is adjusted to satisfy the requisite FMR condition at a given angle. For uniaxial and planar anisotropy materials, however, the larger $4\pi M_s$ values and large anisotropy fields cause the angle between $\mathbf{H}_{ext}$ and $\mathbf{M}_s$ to vary considerably as one sweeps the field through the FMR response curve. This leads to a significant difference in the angle profiles for $\Delta(\omega/\gamma)$ and ΔH in these materials.

The γ, $4\pi M_s$, and H_A values used for the results shown below are the same as those used to calculate the field versus angle and linewidth versus angle results shown in Figs. 2 and 3. The exchange constant D in the spin wave dispersion relations is taken to be independent of the propagation angle and to have a nominal value of 5×10^{-9} Oe cm^2/rad^2, the same value used for the spin wave dispersion relations of Figs. 5–7.

A. Linewidth versus angle profiles: Basic dependences

It will be useful to develop first a qualitative picture for the expected angle dependences and the effect of scatterer size and type on the linewidth versus angle profiles. These issues are best addressed for the case of an isotropic material where $H_A=0$ because of the considerable simplifications to the FMR field and spin wave dispersion expressions which result in this limit.

As a further simplification, the angle dependence of the relaxation rate is easiest to understand for the case of isotropic scattering. The effect of scatterer size on the linewidth versus θ profile will be first examined for this limit. For isotropic scattering, the coupling between the uniform mode and the degenerate spin waves does not depend on the spin wave propagation direction. In this case, the relaxation rate is simply related to the number of degenerate spin waves which lie below the cut-off wave number $k=\pi/R$ and the corresponding weighting of these states according to $[j_1(kR)/kr]^2$ coupling term in the scattering integral. For the case of very small scatterers, such that π/R is much greater than the largest available k value at $\theta=90°$, all of the available degenerate spin waves at a given θ participate equally in the scattering. In this situation, the only consideration which contributes to the angle dependence of the FMR linewidth at constant frequency is the variation in the number of degenerate states with θ. All states out to the largest available k value for the specified θ value, taken as k_{cut}, contribute. These contributions are weighted, of course, according to $[j_1(kR)/kr]^2$.

This effect was shown through the dispersion diagrams in Fig. 5. These same dispersion diagrams are repeated in Fig. 10, along with an additional diagram which shows the resulting two magnon frequency linewidth $1/\gamma T_{TM}$ as a function of θ. Figures 10(a), 10(b), and 10(c) show the spin wave dispersion diagrams for three different field orientations as in Fig. 5. These diagrams include, however, additional vertical dashed lines which indicate the position of the π/R cut-off wave number for two magnon scattering from the $j_1(kR)$ term in the $F(\mathbf{k})$ coupling function of Eq. (23). For very small scatterer sizes, R is also very small and these π/R lines are always outside the spin wave band at the FMR frequency point. This means that the entire band of degenerate states indicated by the shaded horizontal strip of modes in (b) and (c) contributes to the two magnon scattering losses.

Figure 10(d) shows the frequency linewidth as a function of the field angle θ which results. For small angles, the spin wave band is high in frequency, few states are degenerate, and the resulting relaxation rate is small. In the limit $\theta\rightarrow0$, the number of degenerate states goes to zero as well for a thin film of infinite extent, and the two magnon linewidth also goes to zero. As the angle is increased, however, the spin wave band shifts down in frequency relative to the FMR frequency position, more and more states become degenerate with the FMR frequency, and the linewidth increases. As one approaches the parallel field FMR condition at $\theta=90°$, one reaches the configuration with the maximum number of degenerate spin waves and the two magnon linewidth reaches a maximum. It should be emphasized that the linewidth versus

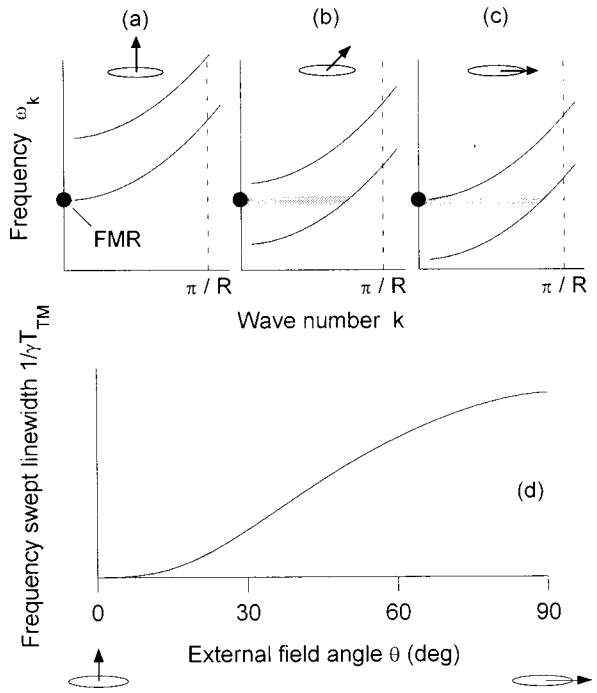

FIG. 10. (a)–(c) show schematic spin wave dispersion curves of spin wave frequency ω_k vs wave number k. These diagrams are for a thin isotropic film and three orientations of the external static field with the sample biased at the static field needed for FMR at some constant frequency, as indicated. These diagrams follow the same format as Fig. 5. For (a) the static field is applied perpendicular to the film plane at $\theta=0°$. For (b) the static field is applied at some intermediate angle. For (c) the static field is applied in the film plane at $\theta=90°$. The shaded horizontal regions in (b) and (c) show the band of available degenerate spin wave states for two magnon scattering in each case. The vertical dashed line at $k=\pi/R$ in each diagram shows the position of the effective wave number associated with an inhomogeneity radius R. For these diagrams, a small size inhomogeneity is assumed, so that the $k=\pi/R$ point is always outside the spin wave band at the FMR frequency. The solid line in (d) shows the variation in the two magnon scattering frequency swept linewidth $1/\gamma T_{TM}$ with the external field angle.

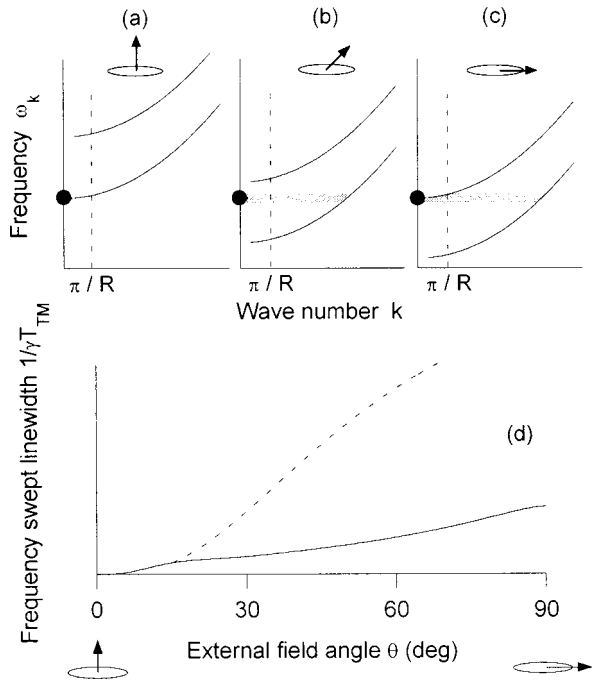

FIG. 11. (a)–(c) show schematic spin wave dispersion curves of spin wave frequency ω_k vs wave number k in the same format and under the same conditions as for Fig. 10. Also as in Fig. 10, the vertical dashed line at $k=\pi/R$ in each diagram shows the position of the effective wave number associated with an inhomogeneity radius R. For these diagrams, however, a large size inhomogeneity is assumed, so that the $k=\pi/R$ point is always inside the spin wave band at the FMR frequency point. The solid line in (d) shows the variation in the two magnon scattering frequency linewidth $1/\gamma T_{TM}$ with the external field angle. The dashed line repeats the small size inhomogeneity result from Fig. 10.

angle profile result in Fig. 10(d) is for: (i) isotropic scattering and (ii) very small scatterer sizes. The profile which results is a reflection of the variation in the number of degenerate spin waves with angle, and no other effects.

For YIG parameters and an FMR frequency in the GHz regime, the results in Fig. 10 would correspond to small scatterers with sizes on the order of 0.05 μm or smaller. If one were to increase the size of the scatterers, one could move the π/R cut-off wave number inside the spin wave band for θ values above some lower limit. This effect, the resulting change in the scattering, and the change in the linewidth versus field profile for a large scatterer size are shown in Fig. 11. The format of Fig. 11 is the same as Fig. 10, with spin wave band diagrams in (a), (b), and (c), and a linewidth versus θ diagram in (d). Note that for (b) and (c), the vertical dashed lines at $k=\pi/R$ are now well inside the spin wave band at the FMR frequency. The solid line in (d) shows the calculated two magnon linewidth versus angle profile and the dashed line repeats the result from Fig. 10(d).

As shown by the kink in the solid curve in Fig. 11(d) near $\theta=15°$ or so, and departure of the solid line from the dashed line at larger θ values, the change from a small scatterer size to a large scatterer size has a drastic effect on the linewidth versus angle profile. At small values of θ, as long as k_{cut} is less than π/R, the two magnon linewidth is the same as in Fig. 10. This result is shown by the part of the solid curve in Fig. 11(d) out to 10° or so. The kink in (d) occurs at the θ value for which $\pi/R=k_{cut}$ is satisfied. For larger θ values, k_{cut} is now greater than π/R. Now, the modes which can contribute to the two magnon scattering truncate at $k=\pi/R$ rather than at k_{cut} and the two magnon linewidth is reduced from the dashed line result in (d) to the solid line result. The space between the solid line and the dashed line in (d) represents those modes between $k=\pi/R$ and $k=k_{cut}$ which are now excluded from the scattering process. As a result, the linewidth continues to increase with angle, but at a lower rate than for the case of small scatterers. The increase in linewidth with θ is now due to the increase in the number of degenerate states for the low k modes only, that is, those modes which satisfy the condition $k<\pi/R$.

The results in Figs. 10 and 11 show how the details of the microstructure affect the two magnon linewidth versus field angle profile for thin films. The truncation effect which is evident from the solid and dashed curves in Fig. 11(d) shows that the size of the scatterer plays a crucial role in shaping these profiles. For the example shown, one can see that the position of the kink in the profile, if such a kink can be observed, (i) indicates a relatively large scatterer size and (ii) provides a direct indication of the size of the scatterer. In the case of YIG parameters, a kink should be observable for

scatterer sizes greater than 0.1 μm or so. Specific numerical results which demonstrate these effects will be shown shortly.

For the isotropic scattering option used for Figs. 10 and 11, all of the degenerate spin waves with $k<\pi/R$ and all the corresponding available θ_k values are taken to scatter equally. If one considers the case of spherical void scattering, one must insert the θ_k dependent scattering factor back into the analysis. Recall that as one moves across the horizontal band of degenerate spin waves indicated by the shaded stripes in (b) and (c) of Figs. 10 and 11, the spin wave angle θ_k is changing. For the diagrams as shown, θ_k is generally decreasing as one moves from lower to higher k values. The presence of the $(3\cos^2\theta_k-1)^2$ term in the scattering integral results in certain spin waves being weighted more heavily than others. This weighting produces additional angle dependences in the linewidth versus field angle θ profiles. Generally, these additional effects are more pronounced for large scatterer sizes than for small scatterers.

For small scatterers, as indicated above, all of the degenerate modes across the band must be considered. One has, in effect, an average of the additional $(3\cos^2\theta_k-1)^2$ angle factor over all the available k values from zero to $k_{\rm cut}$. This will tend to smear out the explicit θ_k dependences which are introduced through the $(3\cos^2\theta_k-1)^2$ factor. When the scatterer radius R is large, on the other hand, the scattering contributions become limited to relatively low wave numbers which satisfy $k<\pi/R\ll k_{\rm cut}$ over all but the smallest values of the field angle θ. This limitation translates to the selection of a small range of θ_k values for each θ value which generally ranges from $\theta_k\approx 0°$ at $\theta=0°$ to $\theta_k\approx 90°$ at $\theta=90°$. In this limit, the $(3\cos^2\theta_k-1)^2$ coupling term for spherical void scattering can dominate the linewidth versus θ profile character.

B. Linewidth angle profiles for thin and thick YIG films

Figure 12 shows numerical results for the effects just discussed. The graphs show the calculated two magnon scattering frequency linewidth $\Delta(\omega/\gamma)=1/\gamma T_{\rm TM}$ as a function of external field angle θ for a YIG film of infinite extent. At each θ value, the external field was adjusted for an FMR frequency of 10 GHz. The YIG material and microwave parameters were taken to be the same as those used for the numerical results shown earlier. Figure 12(a) is for scatterers with a radius $R=0.04$ μm. Figure 12(b) is for scatterers with a radius $R=0.1$ μm. Figure 12(c) is for scatterers with a radius $R=0.2$ μm. These particular R values were chosen to demonstrate the role of the scatterer size on the linewidth profiles. The isotropic scattering results are shown by the solid lines and the results for spherical void scattering are shown by the dashed lines. The ratio of the total scatterer volume to the sample volume p was always taken to be 0.01, for a nonmagnetic volume of 1%.

Consider the results for the isotropic scattering model first. For the smallest inhomogeneity size, $R=0.04$ μm, the solid curve in (a) shows that the relaxation rate increases steadily with field angle. In this case, the small scatterer size places π/R well above the highest value of k for degenerate

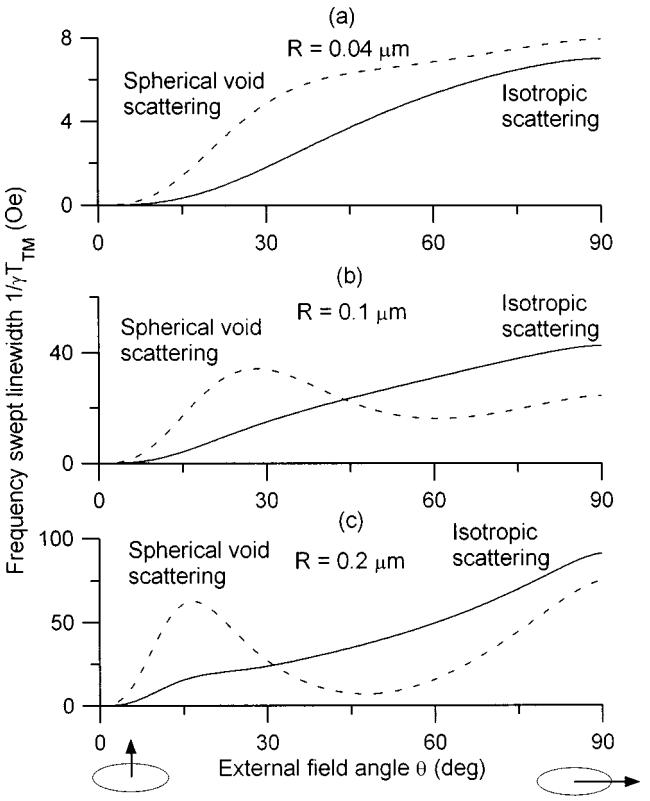

FIG. 12. Calculated two magnon frequency linewidth $1/\gamma T_{\rm TM}$ as a function of the external field angle θ for an isotropic YIG film at 10 GHz in the infinite thin film limit. (a) is for scatterers with a radius $R=0.04$ μm, (b) is for $R=0.1$ μm, and (c) is for $R=0.2$ μm. The porosity parameter p was set at 0.01 for all computations. The solid lines show results for the isotropic scattering approximation and the dashed lines are for spherical void scattering.

modes at $k_{\rm cut}\sim 3.8\times 10^5$ rad/cm for $\theta=90°$. As in Fig. 10, the increase in linewidth with angle shown by the solid line in Fig. 12(a) simply reflects the increase in the number of degenerate states with angle and the k-dependent $[j_1(kR)/kr]^2$ weighting factor in the scattering integral. Turn now to the smallest inhomogeneity size at $R=0.2$ μm and the solid curve in (c). Here, the maximum spin wave wave number for scattering is at $\pi/R=1.6\times 10^5$ rad/cm. This k value is well below the maximum $k_{\rm cut}$ value cited above. In accord with the Fig. 11 discussion, one now observes a distinct kink in the linewidth versus angle profile. This kink is evident for the solid curve in Fig. 12(c) at a θ value near 15°. This kink point corresponds to the angle at which the condition $k_{\rm cut}\sim\pi/R$ is satisfied. The solid curve in (b) for $R=0.1$ μm represents an intermediate situation. While the shape of the solid curve profile is different from that in (a), the change in character at the $k_{\rm cut}\sim\pi/R$ is not as pronounced.

It is important to take not of the different vertical axis scales for the graphs in Fig. 12. From (a) to (b) to (c), this scale increases from 0–8 Oe to 0–50 Oe to 0–100 Oe. The growth in the two magnon linewidth as R is increased is due mainly to the R^3 factor in Eq. (27). The increase does not scale strictly with the cube of the scatterer size because of the decrease in the π/R cut-off point in wave number as R is increased.

Turn now to the results for spherical void scattering, shown by the dashed lines. The linewidth versus angle profiles now show more complicated variations than for isotropic scattering. Note, in particular, the appearance of a pronounced shoulder in dashed line profile in (a) and the broad peaks in the 15°–30° range for (b) and (c). The (b) and (c) results show that these peaks become somewhat sharper and shift to smaller θ values as the scatterer size is made larger. For the largest R value and (c), the dashed curve provides a reasonable representation of the $(3\cos^2\theta_k - 1)^2$ coupling, in which the spin wave θ_k propagation angle at low k maps more-or-less into the variation in the field angle θ. The calculated linewidth in (c) for the larger scatterers is similar to the angle dependence shown in Fig. 3 of Ref. 18.

The results in Fig. 12, as well as most of the considerations in previous sections, have been for the case of an infinite thin film where the sample demagnetizing factors are given by $N_Z = 1$ and $N_{XY} = 0$. One result, as shown in Figs. 10–12, is that the two magnon linewidth vanishes in the limit of a film magnetized perpendicular to the film plane. This is true because the FMR point then lies at the bottom of the band and there are no degenerate spin wave states to contribute to the scattering. This is not the situation for a film for which N_Z is no longer unity and N_{XY} is no longer zero.

It is instructive to consider modifications to the two magnon linewidth versus angle profiles for the case of a finite size film or disk, where $N_Z < 1$ and $N_{XY} > 0$ are satisfied. The results are shown in Fig. 13. The calculations were made with the same YIG material and FMR parameters as for Fig. 12, a scatterer radius R of 0.04 μm, spherical void scattering, and two different disk diameter d to disk thickness S aspect ratios, $d/S = 100$ and $d/S = 10$. Numerical values for the demagnetizing factors can be found by the Osborn method.[40] Figures 13(a) and 13(b) show spin wave bands for the two cases, as indicated, and the effect of disk size on the two magnon frequency linewidth $1/\gamma T_{\mathrm{TM}}$ versus field angle θ profile is shown in (c). The solid and dashed curves in Fig. 13 show the two magnon linewidth versus angle for thin film $d/S = 100$ case and the thick film $d/S = 10$ case, respectively.

The format for the spin wave band diagrams in (a) and (b) is the same as for previous graphs. The top and bottom solid curves show the bulk spin wave frequency ω_k versus wave number k for $\theta_k = 90°$ and $\theta_k = 0°$, respectively. For purposes of comparison, these diagrams are shown for one common value of the static internal field. The positions of the FMR frequencies when the corresponding external field is oriented at $\theta = 0°$ and $\theta = 90°$ are shown by the horizontal dashed lines labeled with the small disk diagrams with either a perpendicular arrow or an in-plane arrow, respectively. For the thin film $d/S = 100$ case and Fig. 13(a), the two FMR frequencies are at the bottom and the top of the $k = 0$ band limits, as expected. For the thick film $d/S = 10$ case and Fig. 13(b), the two FMR frequencies are no longer at the $k = 0$ band limits. As already indicated, this change affects the two magnon linewidth versus angle profile significantly.

The effects of finite size on the two magnon linewidth are clear from the curves in Fig. 13(c). The solid curve is essentially the same as shown in Fig. 12(a). The dashed curve for the thick film case shows a modified profile. This

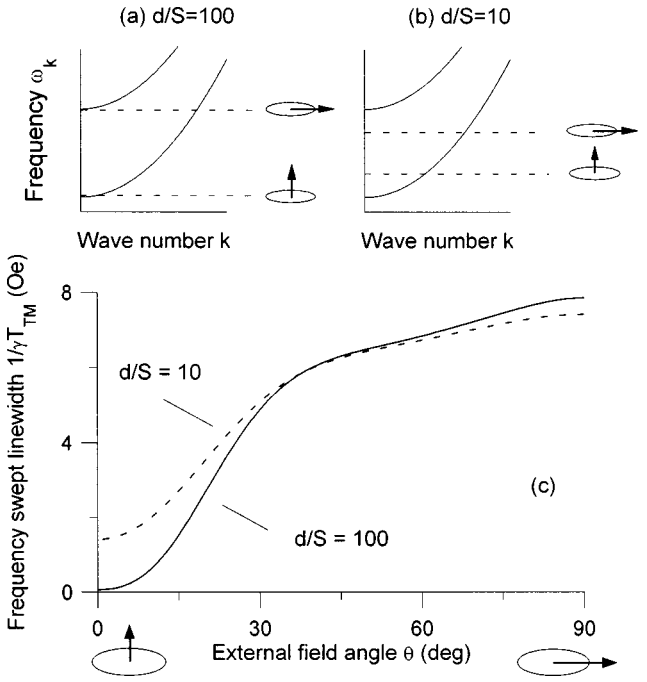

FIG. 13. (a) and (b) show schematic spin wave dispersion curves of spin wave frequency ω_k vs wave number k which illustrate the relative FMR frequencies and spin wave band position at a fixed value of the static field for two different film diameter d to thickness S ratios. (a) is for a d/S ratio of 100. (b) is for $d/S = 10$. The upper and lower horizontal dashed lines in these diagrams show the FMR frequency for the in-plane static field and perpendicular-to-field configurations, as indicated. (c) shows calculated frequency linewidths for a YIG film or disk at an FMR frequency of 10 GHz as a function of the external field angle θ for 0.04 μm scatterers and spherical void scattering. The solid curve is for a relatively thin slab with $d/S = 100$. The dashed curve is for a relatively thick slab with $d/S = 10$. The porosity parameter p was set at 0.01.

curve no longer goes to a zero linewidth in the perpendicular $\theta = 0°$ limit and has a slightly reduced value in the parallel $\theta = 90°$ limit. These changes are due to the relative shifts in the FMR frequency positions relative to the spin wave band for the thicker film. Note that the basic profile has the same character. This is because the basic evolution in the density of states with the external field angle θ has not changed.

C. Linewidth versus angle profiles for Ba–M and Zn–Y

The effects of inhomogeneity size, type of scattering interaction, and film thickness on the angle dependence of the two magnon linewidth for isotropic films hold for the uniaxial materials as well. Here, however, there are additional complications for both the uniform mode FMR response and the spin wave dispersion relations.

For an easy-axis material such as Ba–M, there are two main effects. First, the anisotropic distortion of the top of the spin wave band shown in Figs. 6 and 9 has a significant effect on the number of degenerate modes available for scattering as one moves from the perpendicular FMR condition at $\theta = 0°$ to the parallel FMR condition at $\theta = 90°$. Note, in particular, that the FMR position moves from the very bottom of the spin wave band for $\theta = 0°$, through the bottom of the top spin wave band surface at $\theta_k = 90°$ and $\phi_k = 0°$ for

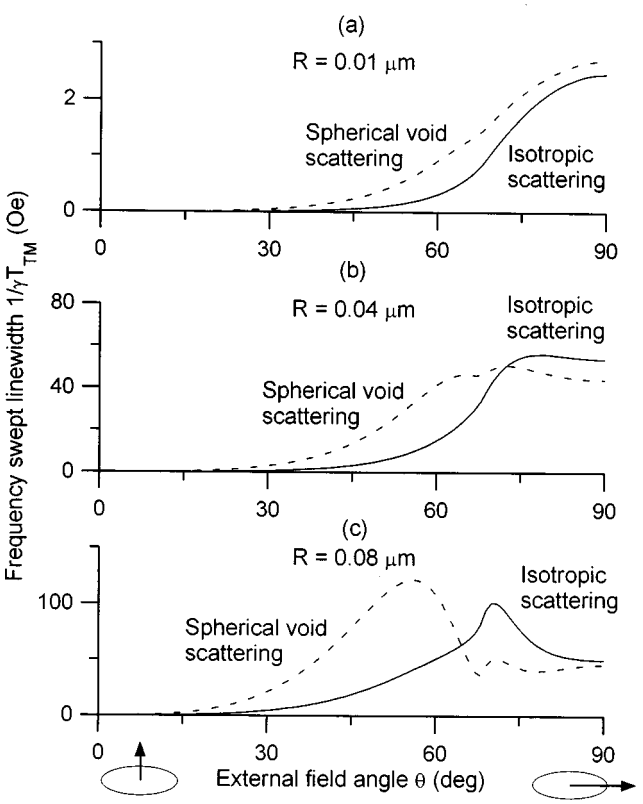

FIG. 14. Calculated two magnon frequency linewidth $1/\gamma T_{TM}$ as a function of the external field angle θ for an easy axis Ba–M film at 50 GHz in the infinite thin film limit. The easy axis is perpendicular to the film plane. (a) is for scatterers with a radius $R=0.01$ μm, (b) is for $R=0.04$ μm, and (c) is for $R=0.08$ μm. The porosity parameter p was set at 0.01 for all computations. The solid lines show results for the isotropic scattering approximation and the dashed lines are for spherical void scattering.

some intermediate θ value, and then to the very top of the band at $\theta_k=90°$ and $\phi_k=90°$ for $\theta=90°$. Second, the effects which derive from this movement of the FMR point from the bottom of the band to the top of the band become compressed in angle. Subject to the constraint of a constant FMR frequency, the large uniaxial anisotropy tends to hold the magnetization angle ϕ at values close to 0° until θ becomes relatively large. Most of the rotation of the static magnetization and the corresponding change in ϕ takes place for $45°<\theta<90°$.

The above effects are demonstrated by the numerical results on the frequency swept two magnon linewidth versus field angle in Fig. 14. The calculations were based on the same Ba–M parameters cited above and for an FMR frequency of 50 GHz. Figure 14(a) is for scatterers with $R=0.01$ μm, 14(b) is for $R=0.04$ μm, and 14(c) is for $R=0.08$ μm. The porosity parameter p was taken as 0.01 for all graphs. Curves for isotropic scattering and spherical void scattering are shown by the solid and dashed lines, respectively, in each graph.

Consider the isotropic scattering results first. For very small scatterers and $R=0.01$ μm, as in (a), the linewidth versus angle profile is similar to that for the isotropic YIG material in Fig. 12(a). The only real difference is that the main field angle effects have been pushed to large θ values. This is due to the rotation effects noted above. If the horizontal axis displayed the magnetization angle ϕ rather than the field angle θ, the profile would be very close to that shown in Fig. 12(a). As the size of the scatterer is increased, however, there are some significant new dependences. The solid curves in Fig. 14(b) and Fig. 14(c) show that the increase in R is accompanied by the development of a pronounced high angle peak. This high angle peak has nothing to do with the spherical void scattering θ_k-dependent scattering which produced the low angle peak shown by the dashed curves in Fig. 12. This high angle isotropic scattering peak for the Ba–M films is due to the distortion of the top of the spin wave band as illustrated in Figs. 6 and 9, coupled with drop in π/R to values well below k_{cut}. The $f(k)$ function which gives the minimum ϕ_k for scattering becomes nonzero when the FMR frequency cut is across the warped $\theta_k=90°$ top surface of the spin wave band, as in Figs. 6(c), 6(d), and 9. When this occurs, there is a loss of degenerate states at low wave numbers. If only low k states can be coupled, as is the case when π/R is small, this results in a decrease in linewidth. This is the origin of the peak in linewidth at $\theta\sim70°$ shown by the solid curve in Fig. 14(c).

The spherical void scattering results are shown by the dashed lines in the graphs of Fig. 14. All of the previous discussion for isotropic scattering in the Ba–M film apply here as well. The profiles are pushed over to higher θ values and there is a high θ peak associated with the warped top surface of the spin wave band and the minimum ϕ_k effect. Now, however, this peak is somewhat obscured by the peak at lower θ values which comes in for spherical void scattering when R is large. This lower θ peak is directly related to the $(3\cos^2\theta_k-1)^2$ contribution to the scattering in Eq. (27). Here too, the previous discussion for the YIG film applies. The peak in linewidth near $\theta=55°$, evident from the dashed curve in Fig. 14(c), derives from this term. As with the YIG example, the small value of π/R serves to select out a narrow range of θ_k values which allow the linewidth versus the field angle θ to reflect this coupling in an almost one-to-one manner.

As a final example, consider the case of an easy-plane anisotropic material. Figure 15 shows calculated two magnon scattering linewidths as a function of external field angle for a Zn–Y film in the infinite thin film limit and for ferromagnetic resonance at 10 GHz. Figure 15(a) is for $R=0.04$ μm and 15(b) is for $R=0.1$ μm. As with the two previous figures, the results for isotropic scattering and spherical void scattering are shown by the solid lines and the dashed lines, respectively. The p value was 0.01. The Zn–Y parameters were the same as cited previously.

Consider the isotropic scattering results first. The solid lines in the graphs of Fig. 15 appear at first glance to be quite different from either of the two previous examples. For both of the R values examined, the two magnon linewidth increases very rapidly from zero to $\theta=0°$ to a relatively constant value for θ values above 10°–15° or so. This initial rapid increase with θ is somewhat misleading, however. For this easy plane material, the anisotropy serves to enhance the tendency for the static magnetization vector to lie in-plane. As the external field angle is moved away from 0°, the magnetization angle ϕ moves from 0° to angles close to 90°

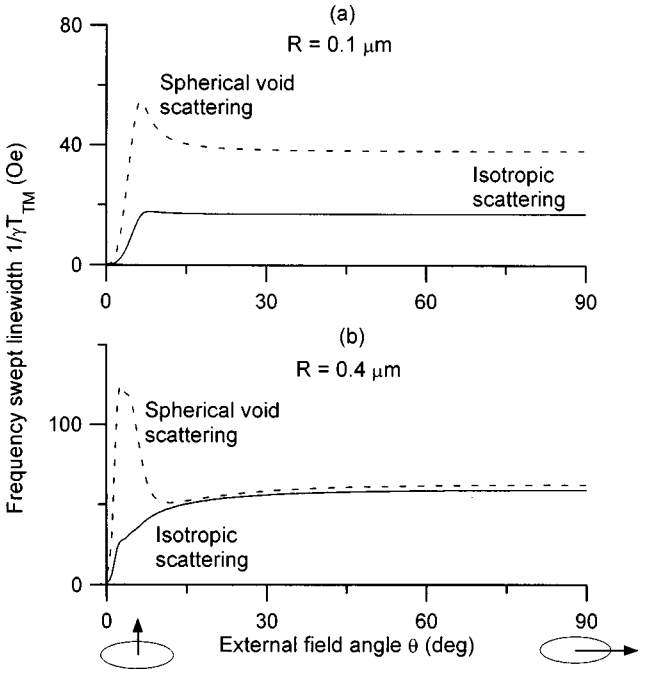

FIG. 15. Calculated two magnon frequency linewidth $1/\gamma T_{TM}$ as a function of the external field angle θ for an easy plane Zn–Y film at 10 GHz in the infinite thin film limit. The easy plane is the film plane. (a) is for scatterers with a radius $R=0.1$ μm and (b) is for $R=0.4$ μm. The porosity parameter p was set at 0.01 for all computations. The solid lines show results for the isotropic scattering approximation and the dashed lines are for spherical void scattering.

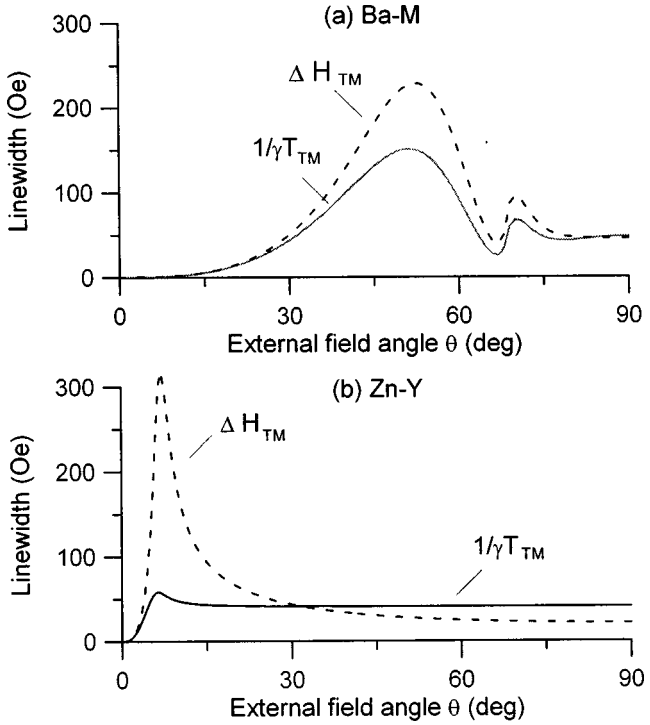

FIG. 16. Diagrams of calculated two magnon frequency linewidth $1/\gamma T_{TM}$ and the corresponding field swept two magnon linewidth ΔH_{TM} as a function of the external field angle θ. (a) is for an easy axis Ba–M film at 50 GHz in the infinite thin film limit. (b) is for an easy plane Zn–Y film at 10 GHz in the infinite thin film limit. Both diagrams are for scatterers with a radius $R=0.1$ μm, a porosity parameter p of 0.01, and spherical void scattering. The dashed lines show the results for the frequency swept linewidth $1/\gamma T_{TM}$. The solid lines show the results for the field swept linewidth ΔH_{TM}.

rather quickly. This is a result of the large easy-plane anisotropy together with the demagnetization fields which act to pull the magnetization vector in the plane of the film even for relatively low values of the external field angle. For the results in Fig. 15, the range of θ values from 0° to 15° corresponds to a change in ϕ from 0° to nearly 90°. If these linewidths were displayed as a function of ϕ, the profiles in Fig. 15 would have a very similar appearance to the profiles in Fig. 12 for YIG films. Most of the YIG discussion applies here as well. The small shoulder at $\theta\sim 3°$ on the solid curve Zn–Y result in Fig. 15(b) for $R=0.1$ μm, for example, is related to the same $k_{cut}=\pi/R$ condition which caused the shoulder to appear on the solid curve in Fig. 12(c). Here, the shoulder occurs at a much smaller θ value because of the planar anisotropy.

For spherical void scattering, the effects also track the results for the YIG films in terms of the ϕ rotation. The single peak which is evident for both of the dashed curves in Fig. 15 is due to the $(3\cos^2\theta_k-1)^2$ term in Eq. (27). The peak is more distinct for the larger R value. This is because the reduced coupling to modes with k values above π/R tends to select out a more limited range of θ_k values for the scattering, and this allows the functional form of the $(3\cos^2\theta_k-1)^2$ coupling term to be reflected directly in the linewidth versus θ response. The arguments here are exactly the same as for the YIG case.

It is important to note that for Zn–Y there is no additional peak at higher θ values associated with the warped top $\theta_k=90°$ surface of the spin wave band, as was the case for the Ba–M analysis. For ferromagnetic resonance in a c-plane film of Zn–Y, the resonance frequency lies at the bottom of the spin wave band for $\theta=0°$, but then moves only to the bottom of the warped surface of the band at $\theta=90°$. This result was emphasized in connection with Fig. 7. For Ba–M films, the FMR frequency cut moves into the warped part of the band for large θ values. This is not the case for Zn–Y.

The above YIG, Ba–M, and Zn–Y examples demonstrate explicitly the various processes which can affect the two magnon linewidth. There are density of states effects. There are anisotropy effects. There are microstructure effects. There is one final effect to be considered, the difference between the frequency swept linewidth $\Delta(\omega/\gamma)$ and the field swept linewidth ΔH. Recall that there is, in general, a variation in the field swept linewidth ΔH with the field angle θ even for a constant $\Delta(\omega/\gamma)$. This point was made explicitly in connection with Fig. 3. The effect was relatively small for YIG materials, about a 50% effect for Ba–M materials, and an over 600% effect for Zn–Y films.

It is only necessary to consider the differences between $\Delta(\omega/\gamma)$ and ΔH for the Ba–M and Zn–Y cases. Figure 3(a) shows that the effect is small for YIG films. Figure 16 shows a comparison of frequency swept and the corresponding field swept two magnon linewidth versus field angle profiles for Ba–M and Zn–Y thin films. Figure 16(a) is for Ba–M at 50 GHz. Figure 16(b) is for Zn–Y at 10 GHz. In both cases, the calculations were based on a scatterer size of 0.1 μm, the infinite thin film limit, spherical void scattering, and a poros-

ity p parameter of 0.01. The dashed lines show the two magnon frequency swept linewidth $\Delta(\omega/\gamma)=1/\gamma T_{\mathrm{TM}}$ angle profiles. The solid lines show the two magnon field swept linewidth ΔH_{TM} profiles. The field swept linewidths were obtained from the frequency swept two magnon linewidths and Eq. (10), with the FMR derivative factor $\gamma\partial H_{\mathrm{FMR}}/\partial\omega_{\mathrm{FMR}}$ evaluated numerically at each θ. From the results in Fig. 3, it is evident that this factor is equal to one at $\theta=0°$, greater than one when $\mathbf{M}_s$ rotation effects are important at intermediate angles, and less than one for resonance when the static field is in plane at $\theta=90°$.

The results in Fig. 16 are self explanatory. In the Ba–M case, the roughly 50% effect at $\theta\sim 60°$ from Fig. 3 serves mainly to magnify the angle profile for ΔH_{TM}. The basic profile structure found for $1/\gamma T_{\mathrm{TM}}$ is retained. Although it is not readily evident from the curves shown, the field swept linewidth at $\theta=90°$ is slightly smaller than the frequency swept linewidth. This is a direct consequence of the fact that the rotation effects for θ values different from 0° and 90° cause $\gamma\partial H_{\mathrm{FMR}}/\partial\omega_{\mathrm{FMR}}$ to be greater than unity and to broaden the field swept FMR line, while dynamic demagnetizing effects which affect the FMR frequency field equation at $\theta=90°$ give a $\gamma\partial H_{\mathrm{FMR}}/\partial\omega_{\mathrm{FMR}}$ multiplier which is less than unity.

The situation is quite different for Zn–Y. Here, the 600% effect for the $1/\gamma T_{\mathrm{TM}}$ to ΔH_{TM} conversion, combined with relatively sharp peaks for both $1/\gamma T_{\mathrm{TM}}$ and $\gamma\partial H_{\mathrm{FMR}}/\partial\omega_{\mathrm{FMR}}$ over roughly the same range in θ values, leads to a very significant change. One finds that (i) the peak in ΔH_{TM} is accentuated to the extreme and shifted in θ, and (ii) the ΔH_{TM} for large values of θ actually falls below $1/\gamma T_{\mathrm{TM}}$. For Zn–Y, this decrease in ΔH_{TM} below $1/\gamma T_{\mathrm{TM}}$ at large θ is much more distinct than for Ba–M, as was also the case in Fig. 3.

VI. ADDITIONAL CONSIDERATIONS

As discussed in Sec. I, an important consideration which has been neglected in this work involves the effect of film thickness on the normal spin wave modes. For thin films, the bulk spin wave dispersion relations are not the true normal modes of the system, due to the film surfaces and the corresponding boundary conditions on the dynamic magnetization. Instead of the continuous spectra of spin wave dispersion curves within the band, the spin wave spectrum is discretized. One would then expect the angle dependence of the linewidth to reflect the discrete nature of the normal modes. The dipole-exchange mode dispersion relations developed by Kalinikos *et al.*[36] for obliquely magnetized anisotropic thin films, for example, might be used in place of the bulk dispersion relations in order to determine the effect of film thickness.

There are a number of additional considerations which may be important in the two magnon calculation but have been neglected in this analysis. First, the exchange constant D has been taken to be independent of propagation angle. As mentioned above, this may not be the case for highly anisotropic Ba–M hexagonal ferrite materials. Second, the effect of the ellipticity of the uniform mode and the spin wave has also been neglected. It is reasonable to expect that the ellipticity would influence the coupling between the inhomogeneities and the degenerate spin waves. Third, a scattering Hamiltonian based on fluctuations in the effective anisotropy field H_A rather than the saturation induction $4\pi M_s$ might provide a better model of the microstructure in highly anisotropic ferrites.

VII. SUMMARY

The two magnon scattering contribution to the ferromagnetic resonance relaxation rate and linewidth has been evaluated as a function of field angle for isotropic and anisotropic disks and films. The analysis was based on the original SLK treatment but has been extended to include anisotropic materials, nonspherical scatterers, sample demagnetization factors, and a nonzero linewidth for the scattered spin wave modes. The analysis yields characteristic angle dependences in the two magnon scattering linewidth which reflect the scatterer size, sample shape, scattering interaction, and crystalline anisotropy. Specific numerical evaluations were done for three types of materials: YIG, Ba–M, and Zn–Y. These explicit calculations serve to demonstrate the various effects of the spin wave band shift relative to the FMR frequency, anisotropy, and microstructure on the two magnon relaxation process. The results demonstrate that measurement of the FMR linewidth as a function of angle for film and disk materials can provide useful information on the microstructure and two magnon losses in the sample.

ACKNOWLEDGMENTS

The authors acknowledge Dr. P. Kabos, Dr. B. A. Kalinikos, Dr. M. A. Wittenauer, and Dr. A. K. Srivastava for helpful discussions during the course of this study. Dr. A. K. Srivastava provided a critical reading of the final manuscript. This work was supported, in part, by the United States Office of Naval Research Grant Nos. N00014-94-1-0096 and N00014-91-J-1324, the United States Army Research Office, Grant No. DAAH04-95-1-0325, and the National Science Foundation, Grant No. DMR-9400276.

[1] See, for example, F. Bertaut and F. Forrat, C. R. Acad. Sci. **242**, 382 (1956); G. Giello and M. A. Gilleo, Acta Crystallogr. **10**, 239 (1957).
[2] C. E. Patton, in *Magnetic Oxides*, edited by D. J. Craik (Wiley, London, 1975), Ch. 10, pp. 575–645.
[3] M. Sparks, *Ferromagnetic Relaxation Theory* (McGraw-Hill, New York, 1959).
[4] M. Sparks, R. Loudon, and C. Kittel, Phys. Rev. **122**, 791 (1961).
[5] H. B. Callen, J. Phys. Chem. Solids **4**, 256 (1958).
[6] R. C. Fletcher, R. C. LeCraw, and E. G. Spencer, Phys. Rev. **117**, 955 (1960).
[7] E. Schlömann, A.I.E.E. Special Pub. **T-91**, 600 (1956).
[8] M. Motizuki, M. Sparks, and P. E. Seiden, Phys. Rev. **140**, A972 (1965).
[9] E. Schlömann, Phys. Rev. **182**, 632 (1969).
[10] C. R. Buffler, J. Appl. Phys. **30**, 172S (1959); **31**, 222S (1960).
[11] M. Mita, J. Phys. Soc. Jpn. **22**, 529 (1967).
[12] J. Nemarich, Phys. Rev. **136**, A1657 (1964).
[13] A. S. Risley and H. E. Bussey, J. Appl. Phys. **35**, 896 (1964).
[14] A. S. Risley, E. G. Johnson, and H. E. Bussey, J. Appl. Phys. **37**, 656 (1966).
[15] C. E. Patton, C. H. Wilts, and F. B. Humphrey, J. Appl. Phys. **38**, 1358 (1967).
[16] C. E. Patton, J. Appl. Phys. **39**, 3060 (1968).
[17] M. Sparks, Phys. Rev. **1**, B3856 (1969).

[18] M. J. Hurben, D. R. Franklin, and C. E. Patton, J. Appl. Phys. **81**, 7458 (1997).
[19] P. E. Seiden and M. Sparks, Phys. Rev. **137**, A1279 (1965).
[20] J. Sage, Phys. Rev. **185**, 859 (1969).
[21] E. Schlömann, R. I. Joseph, and I. Bady, J. Appl. Phys. **34**, 672 (1963).
[22] C. E. Patton and W. Jantz, IEEE Trans. Magn. **14**, 698 (1978).
[23] C. E. Patton, Phys. Status Solidi B **92**, 211 (1979).
[24] C. E. Patton, Phys. Status Solidi B **93**, 63 (1979).
[25] C. Vittoria, J. Magn. Magn. Mater. **21**, 109 (1980).
[26] P. C. Dorsey, R. Seed, C. Vittoria, D. B. Chrisey, C. Carosella, P. Lubitz, and J. S. Horwitz, IEEE Trans. Magn. **28**, 3216 (1992).
[27] P. C. Dorsey, S. E. Bushnell, R. G. Seed, and C. Vittoria, IEEE Trans. Magn. **29**, 3069 (1993).
[28] F. J. Cadieu, R. Rani, W. Mendoza, B. Peng, S. A. Shaheen, M. J. Hurben, and C. E. Patton, J. Appl. Phys. **81**, 4801 (1997).
[29] C. Kittel, Phys. Rev. **73**, 155 (1948).
[30] N. Bloembergen, Phys. Rev. **78**, 572 (1950).
[31] W. H. von Aulock, *Handbook of Microwave Ferrite Materials* (Academic, New York, 1965).
[32] L. Landau and E. Lifshitz, Phys. Z. Sowjetunion **8**, 153 (1935).
[33] B. Lax and K. J. Button, *Microwave Ferrites and Ferrimagnetics* (McGraw-Hill, New York, 1962).
[34] T. Wolfram and R. E. De Wames, Phys. Rev. B **4**, 3125 (1971).
[35] R. E. De Wames and T. Wolfram, J. Appl. Phys. **41**, 987 (1970).
[36] B. A. Kalinikos, M. P. Kostylev, N. V. Kozhus, and A. N. Slavin, J. Phys.: Condens. Matter **2**, 9861 (1990).
[37] M. J. Hurben and C. E. Patton, J. Magn. Magn. Mater. **139**, 263 (1995).
[38] See, for example, V. Kambersky and C. E. Patton, Phys. Rev. B **11**, 2668 (1975).
[39] C. W. Haas and H. B. Callen, in *Magnetism*, edited by G. T. Rado and H. Suhl (Academic, New York, 1963).
[40] J. A. Osborn, Phys. Rev. **67**, 351 (1945).